Monthly Notices of the ROYAL ASTRONOMICAL SOCIETY

MNRAS **516,** 4862–4881 (2022) https://doi.org/10.1093/mnras/stac2524
Advance Access publication 2022 September 8

A measurement of Hubble's Constant using Fast Radio Bursts

C. W. James [1]★ E. M. Ghosh,[2] J. X. Prochaska,[3,4] K. W. Bannister,[5] S. Bhandari [5,6,7,8] C. K. Day,[9,10] A. T. Deller [10] M. Glowacki [1] A. C. Gordon,[11] K. E. Heintz [12] L. Marnoch,[5,13,14] S. D. Ryder [13,14] D. R. Scott,[1] R. M. Shannon[10] and N. Tejos[15]

[1]*International Centre for Radio Astronomy Research, Curtin University, Bentley, WA 6102, Australia*
[2]*Indian Institute of Science Education and Research Mohali, Knowledge City, Sector 81, SAS Nagar, Manauli PO 140306, India*
[3]*Department of Astronomy and Astrophysics, University of California, Santa Cruz, CA 95064, USA*
[4]*Kavli Institute for the Physics and Mathematics of the Universe, The University of Tokyo, 5-1-5 Kashiwanoha, Kashiwa 277-8583, Japan*
[5]*CSIRO, Space and Astronomy, PO Box 76, Epping NSW 1710 Australia*
[6]*ASTRON, Netherlands Institute for Radio Astronomy, Oude Hoogeveensedijk 4, NL-7991 PD Dwingeloo, the Netherlands*
[7]*Joint institute for VLBI ERIC, Oude Hoogeveensedijk 4, NL-7991 PD Dwingeloo, the Netherlands*
[8]*Anton Pannekoek Institute for Astronomy, University of Amsterdam, Science Park 904, NL-1098 XH, Amsterdam, the Netherlands*
[9]*Department of Physics, McGill University, Montreal, Quebec H3A 2T8, Canada*
[10]*Centre for Astrophysics and Supercomputing, Swinburne University of Technology, PO Box 218, Hawthorn, VIC 3122, Australia*
[11]*Center for Interdisciplinary Exploration and Research in Astrophysics and Department of Physics and Astronomy, Northwestern University, 2145 Sheridan Road, Evanston, IL 60208-3112, USA*
[12]*Cosmic Dawn Center (DAWN), Niels Bohr Institute, University of Copenhagen, Jagtvej 128, DK-2100 Copenhagen ø, Denmark*
[13]*School of Mathematical and Physical Sciences, Macquarie University, NSW 2109, Australia*
[14]*Astronomy, Astrophysics and Astrophotonics Research Centre, Macquarie University, Sydney, NSW 2109, Australia*
[15]*Instituto de Física, Pontificia Universidad Católica de Valparaíso, Casilla 4059, Valparaíso, Chile*

Accepted 2022 September 1. Received 2022 August 13; in original form 2022 June 6

ABSTRACT

We constrain the Hubble constant H_0 using Fast Radio Burst (FRB) observations from the Australian Square Kilometre Array Pathfinder (ASKAP) and Murriyang (Parkes) radio telescopes. We use the redshift-dispersion measure ('Macquart') relationship, accounting for the intrinsic luminosity function, cosmological gas distribution, population evolution, host galaxy contributions to the dispersion measure ($\mathrm{DM_{host}}$), and observational biases due to burst duration and telescope beamshape. Using an updated sample of 16 ASKAP FRBs detected by the Commensal Real-time ASKAP Fast Transients (CRAFT) Survey and localized to their host galaxies, and 60 unlocalized FRBs from Parkes and ASKAP, our best-fitting value of H_0 is calculated to be 73^{+12}_{-8} km s^{-1} Mpc^{-1}. Uncertainties in FRB energetics and $\mathrm{DM_{host}}$ produce larger uncertainties in the inferred value of H_0 compared to previous FRB-based estimates. Using a prior on H_0 covering the 67–74 km s^{-1} Mpc^{-1} range, we estimate a median $\mathrm{DM_{host}} = 186^{+59}_{-48}$ pc cm^{-3}, exceeding previous estimates. We confirm that the FRB population evolves with redshift similarly to the star-formation rate. We use a Schechter luminosity function to constrain the maximum FRB energy to be $\log_{10}E_{\mathrm{max}} = 41.26^{+0.27}_{-0.22}$ erg assuming a characteristic FRB emission bandwidth of 1 GHz at 1.3 GHz, and the cumulative luminosity index to be $\gamma = -0.95^{+0.18}_{-0.15}$. We demonstrate with a sample of 100 mock FRBs that H_0 can be measured with an uncertainty of ± 2.5 km s^{-1} Mpc^{-1}, demonstrating the potential for clarifying the Hubble tension with an upgraded ASKAP FRB search system. Last, we explore a range of sample and selection biases that affect FRB analyses.

Key words: cosmological parameters – fast radio bursts.

1 INTRODUCTION

Fast radio bursts (FRBs) are millisecond-duration pulses of radio emission observed at frequencies from ∼100 MHz up to a ∼8 GHz, now known to originate at cosmological distances (Lorimer et al. 2007; Gajjar et al. 2018; Shannon et al. 2018; CHIME/FRB Collaboration et al. 2021; Pleunis et al. 2021a). Their progenitors and burst production mechanism are as yet unknown and many progenitor models have been proposed (Platts et al. 2019). FRBs have also been observed to repeat (e.g. Spitler et al. 2016) with two showing cyclical phases of irregular activity (Chime/Frb Collaboration et al. 2020; Rajwade et al. 2020). There is evidence that FRBs come from more than one source class (e.g. Pleunis et al. 2021b), although it is also possible that apparent morphological differences in the time-frequency properties of the FRB population can be produced by a single progenitor (Hewitt et al. 2022).

Despite uncertainties as to their origins, FRBs have the potential to act as excellent cosmological probes to trace the ionized gas and magnetic fields in galaxy haloes, large-scale structure, and the intergalactic medium (McQuinn 2014; Masui & Sigurdson 2015; Caleb, Flynn & Stappers 2019; Madhavacheril et al. 2019;

★ E-mail: clancy.james@curtin.edu.au

Prochaska & Zheng 2019; Lee et al. 2022a). This is because the radio pulse from the burst is dispersed while travelling through the ionized intergalactic medium with the total inferred dispersion measure (DM) being a powerful probe of the column density of ionized electrons along the line of sight. Recently, localized FRBs have been used to resolve the 'missing baryons problem' Macquart et al. (2020), where the probability distribution of observed DM given the redshift z of identified FRB host galaxies is analysed to constrain the total baryon density of the Universe and the degree of galactic baryon feedback.

Additionally, FRBs can be used to measure the value of the Hubble constant. The cosmic expansion rate $\dot{a}(t)$ can be expressed in terms of the Hubble parameter $H(z) = \dot{a}(t)/a(t)$. In a flat ΛCDM cosmology, $H(z)$ (sometimes written as $H_0 = 100\,h\,\mathrm{km\,s^{-1}\,Mpc^{-1}}$) can be expressed as $H(z) = H_0\sqrt{\Omega_\Lambda + \Omega_\mathrm{m}(1+z)^3}$, where H_0 is the Hubble constant, Ω_Λ is the vacuum energy density fraction, and Ω_m is the matter density fraction, at $z = 0$. The value of H_0 characterizes the expansion rate of the Universe at the present time, and determines its absolute distance scale. There has been remarkable progress in improving the accuracy of H_0 measurements from local-Universe measurements with the 10 per cent uncertainty from the *Hubble Space Telescope* (Freedman et al. 2001) improving to less than 1 per cent more recently (e.g. Riess et al. 2016; Suyu et al. 2017). However, there exists a $\sim 4\sigma$ tension between measurements of the Hubble constant inferred from Planck observations of the Cosmic Microwave Background (CMB), which is $H_0 = 67.4 \pm 0.5\,\mathrm{km\,s^{-1}\,Mpc^{-1}}$ (Planck Collaboration VI 2020), and those made from calibrating standard candles such as the expanded sample of local type Ia supernovae (SNe Ia) calibrated by the distance ladder ($H_0 = 73.04 \pm 1.04\,\mathrm{km\,s^{-1}\,Mpc^{-1}}$; Riess et al. 2021). Thus, far studies of observational biases and systematic uncertainties have not alleviated this tension motivating solutions that include involving early or dynamical dark energy, neutrino interactions, interacting cosmologies, primordial magnetic fields, or modified gravity in our understanding of the ΛCDM model, see Abdalla et al. (2022) for a recent review. Therefore, an independent and robust method of measuring H_0 would be a welcome, addition to the tools of physical cosmology.

Analysis of FRB observations offer such an independent and local ($z < 1$) test. Two direct observations of FRBs – DM and the signal-to-noise ratio (SNR) – and one inferred property based on host galaxy associations (redshift, z) provide the set of constraints on H_0. There are two largely independent constraints at work. One is effectively a standard candle analysis. To the extent that the FRB energetics are independent of redshift, an ansatz, the SNR dependence with redshift is sensitive to H_0. This constraint, however, is highly degenerate with the (unknown) intrinsic distribution of FRB energies. The other constraint is set by the cosmic contribution to the FRB DM ($\mathrm{DM_{FRB}}$), referred to as $\mathrm{DM_{cosmic}}$. The average value of $\mathrm{DM_{cosmic}}$, $\langle \mathrm{DM_{cosmic}} \rangle \propto \Omega_b H_0$ and to the extent that $\Omega_b H_0^2$ is precisely measured by CMB and big bang Nucleosynthesis analysis (Planck Collaboration VI 2020; Mossa et al. 2020a), this implies $\langle \mathrm{DM_{cosmic}} \rangle \propto H_0^{-1}$. Therefore, the distribution of $\mathrm{DM_{FRB}}$ and redshifts offer a direct constraint on H_0.

To leverage FRBs, one requires a detailed study of the observed distribution of FRBs in SNR, z, and DM space, $P(z, \mathrm{DM}, \mathrm{SNR})$. James et al. (2022a, hereafter J22a) have developed an advanced model of FRB observations, using the Australian Square Kilometre Array Pathfinder (ASKAP) and Murriyang (Parkes) radio telescope data, accounting for observational biases (due to burst temporal width, DM, and the exact telescope beamshape) to assess $P(z, \mathrm{DM}, \mathrm{SNR})$. They estimated that unlocalized ASKAP FRBs arise from $z < 0.5$ with between a third and a half within $z < 0.1$, and find that above a certain DM, observational biases cause the observed Macquart (DM–z) relation to become inverted, implying that the highest-DM events detected in the unlocalized Parkes and ASKAP samples are unlikely to be the most distant. Thus analyses assuming a one-to-one z–DM relationship may lead to biased results, particularly in this high-DM regime.

In this paper, we extend the model developed by J22a to constrain H_0. The modelling of $P(z, \mathrm{DM}, \mathrm{SNR})$ is described in Section 2, along with the distribution of $\mathrm{DM_{host}}$, $\mathrm{DM_{cosmic}}$, Φ (rate of FRBs per comoving volume), and the FRB luminosity function. The detection efficiency and beamshape sensitivity of the surveys are also taken into consideration to calculate the final distribution of FRBs in (z, DM) space. Our sensitivity to H_0 is described in Section 3. In Section 4, the properties of the FRB sample data used from Parkes and ASKAP radio telescopes is described, where we include a total of 16 ASKAP FRBs localized by the Commensal Real-time ASKAP Fast Transients (CRAFT) Survey. In Section 5, we perform a Bayesian analysis to determine the best-fitting value of H_0 given our data set. In Section 6, we test the validity of our model by creating mock sample surveys, using Monte Carlo simulations and checking whether the best-fitting value of H_0 obtained is close to the truth value of H_0 at which the samples are created. Section 7 contains a discussion on these results and on future prospects of precision cosmology, using an extended FRB data set.

2 FORWARD MODELLING THE $P(z, \mathrm{DM}, \mathrm{SNR})$ DISTRIBUTION OF FRBS

Our study is based on comparing three observables related to FRBs to a forward model: (i) the fast radio burst dispersion measure, $\mathrm{DM_{FRB}}$; (ii) the SNR of the pulse relative to the survey threshold, s; and (iii) when available, the redshift z of the FRB determined by a high-probability association to its host galaxy. Details on these quantities and the observational sample are presented in the following section.

The methodology for our forward model was introduced in J22a and applied to several surveys of FRBs. In this manuscript, we present an extension of their model to analyse H_0. We offer a brief summary of the model here, mainly emphasizing the aspects that vary with H_0, and also detail any updates or changes to the model.

2.1 Dispersion measure

The DM of a radio pulse is the integrated number density of free electrons along the propagation path. This causes a delay between the arrival times of different pulse frequencies ν. As an integral measure, $\mathrm{DM_{FRB}}$ includes contributions from several components, which we model separately. $\mathrm{DM_{FRB}}$ is divided into an 'extra-galactic' contribution, $\mathrm{DM_{EG}}$ and a contribution from the 'local' Universe $\mathrm{DM_{local}}$:

$$\mathrm{DM_{FRB}} = \mathrm{DM_{EG}}(z) + \mathrm{DM_{local}}, \tag{1}$$

where

$$\mathrm{DM_{EG}}(z) \equiv \mathrm{DM_{cosmic}}(z) + \frac{\mathrm{DM_{host}}}{1+z}, \tag{2}$$

and

$$\mathrm{DM_{local}} \equiv \mathrm{DM_{ISM}}(l, b) + \mathrm{DM_{halo}}. \tag{3}$$

which includes respective contributions from the Milky Way's interstellar medium (ISM, $\mathrm{DM_{ISM}}$), its Galactic halo ($\mathrm{DM_{halo}}$), the cosmological distribution of ionized gas ($\mathrm{DM_{cosmic}}$), and the FRB host ($\mathrm{DM_{host}}$). The latter incorporates the host galaxy halo, ISM,

and any contribution from the small-scale environment surrounding the FRB progenitor. The NE2001 model (Cordes & Lazio 2002) is used to estimate $\mathrm{DM_{ISM}}$ (l, b) as a function of Galactic coordinates (l, b), while $\mathrm{DM_{halo}}$ is set to be 50 pc cm^{-3} based on estimates from other works (Prochaska & Zheng 2019; Keating & Pen 2020; Platts, Prochaska & Law 2020). In practice, the $\mathrm{DM_{halo}}$ value is largely degenerate with our model for $\mathrm{DM_{host}}$ (but see our discussion in Section 7). For $\mathrm{DM_{host}}$, we adopt the lognormal probability distribution of J22a with parameters μ_{host} and σ_{host}.

The only significant change to the J22a prescription for DM is on the cosmological contribution $\mathrm{DM_{cosmic}}$ which has an explicit dependence on H_0. Adopting the cosmological paradigm of a flat Universe with matter and dark energy, the average value of $\mathrm{DM_{cosmic}}$ is calculated as (Inoue 2004):

$$\langle \mathrm{DM_{cosmic}} \rangle = \int_0^z \frac{c\bar{n}_e(z')\,\mathrm{d}z'}{H_0(1+z')^2\mathrm{E}(z)} \tag{4}$$

$$\text{with } \mathrm{E}(z) = \sqrt{\Omega_{\mathrm{m}}(1+z')^3 + \Omega_\Lambda}, \tag{5}$$

with $\bar{n}_e$ the mean density of electrons,

$$\bar{n}_e = f_d(z)\rho_b(z)m_p^{-1}\chi_e \tag{6}$$

$$= f_d(z)\rho_b(z)m_p^{-1}(1 - \mathrm{Y_{He}}/2), \tag{7}$$

with $\chi_e = Y_{\mathrm{H}} + Y_{\mathrm{He}}/2 \approx 1 - Y_{\mathrm{He}}/2$ calculated from the primordial hydrogen and helium mass fraction Y_{H} and Y_{He}. This is found to be 0.25 (assumed doubly ionized helium) to high precision by CMB measurements (Planck Collaboration VI 2020); current best estimates are 0.2453 ± 0.0034 (Aver et al. 2021). Furthermore, m_p is the proton mass, $f_d(z)$ is the fraction of cosmic baryons in diffuse ionized gas, and ρ_b is the mass density of baryons defined as

$$\rho_b(z) = \Omega_b\rho_{c,0}(1+z)^3, \tag{8}$$

with $\rho_{c,0}$ the critical density and Ω_b the baryon density parameter.

Throughout the analysis, we adopt the Planck Collaboration VI (2020) set of cosmological parameters except for H_0 and Ω_b (uncertainties in the former are subdominant compared to other sources – see Section 7). Because $\rho_c \equiv 3H_0^2/8\pi G$, (4), (6), and (8) imply

$$\langle \mathrm{DM_{cosmic}} \rangle \propto \bar{n}_e H_0^{-1} \propto \Omega_b H_0. \tag{9}$$

Two complementary methods – (1) deuterium to hydrogen measurements coupled with BBN theory and (2) CMB measurements and analysis – have constrained $\Omega_b H_0^2$ to ≈1 per cent precision (Cooke, Pettini & Steidel 2018; Mossa et al. 2020b). Therefore, we consider $\Omega_b(H_0/100)^2$ a fixed constant of 0.02242 (Planck Collaboration VI 2020).[1] Thus when we vary H_0, Ω_b is adjusted accordingly. This yields

$$\langle \mathrm{DM_{cosmic}} \rangle \propto H_0^{-1}, \tag{10}$$

which we explore further in Section 3.

Regarding $f_d(z)$, we adopt the approach derived in Macquart et al. (2020), which combines estimates for the Universe's baryonic components that do not contribute to $\mathrm{DM_{cosmic}}$ (e.g. stars, stellar remnants, neutral gas). Current estimates yield $f_d(z=0) = 0.844$ with uncertainties of a few per cent (dominated by uncertainties in the initial mass function of stars). Evidence suggests an evolving $f_d(z)$ (Lemos et al. 2022), and we use the implementation in Prochaska et al. (2019a) to describe this. For the current study, the uncertainty in $f_d(z)$ is unimportant, yet it may become a limiting systematic in the era of many thousands of well-localized FRBs, as we discuss further in Section 7.2.

[1]The latest measurement, from primordial deuterium abundances, is $\Omega_b h^2 = 0.02233 \pm 0.00036$ (Mossa et al. 2020a). In future works, we will allow for the small uncertainty in $\Omega_b H_0^2$, but it has a negligible contribution to the current results.

2.2 Rate of FRBs

Our model of the FRB population is primarily described in J22a, much of which is in-turn based on Macquart & Ekers (2018b). Here, we describe only modifications to that model.

2.2.1 Population evolution

We model the rate of FRBs per comoving volume $\Phi(z)$ as a function of redshift, specifically to some power n_{sfr} of the star formation rate according to Macquart & Ekers (2018b),

$$\Phi(z) = \frac{\Phi_0}{1+z}\left(\frac{\mathrm{SFR}(z)}{\mathrm{SFR}(0)}\right)^{n_{\mathrm{sfr}}}, \tag{11}$$

and $\mathrm{SFR}(z)$ from Madau & Dickinson (2014),

$$\mathrm{SFR}(z) = 1.0025738\frac{(1+z)^{2.7}}{1+\left(\frac{1+z}{2.9}\right)^{5.6}}. \tag{12}$$

The motivation for this formalism is to allow a smooth scaling between no source evolution ($n_{\mathrm{sfr}} = 0$), evolution with the SFR ($n_{\mathrm{sfr}} = 1$), and a more-peaked scenario similar to AGN evolution ($n_{\mathrm{sfr}} \sim 2$). The total FRB rate in a given redshift interval dz and sky area $d\Omega$ will also be proportional to the total comoving volume dV,

$$\frac{\mathrm{d}V}{\mathrm{d}\Omega dz} = D_H\frac{(1+z)^2D_A^2(z)}{E(z)}, \tag{13}$$

which depends on the angular diameter distance D_A, as well as Hubble distance $D_H = c/H_0$. Thus for a higher value of Hubble's constant, the rate of FRBs in a comoving volume dV will be lower, assuming the SFR remains constant.

2.2.2 FRB luminosity function

In J22a, we modelled the FRB luminosity function by a simple power-law distribution $p(E) \propto E^\gamma$ bounded by a minimum and maximum energy (E_{min}, E_{max}). We use 'burst energy' as the isotropic equivalent energy at 1.3 GHz (i.e. beaming is ignored), and use an effective bandwidth of 1 GHz when converting between spectral and bolometric luminosity. While we find this simple distribution is still a sufficient description of the observational data, we now adopt an upper incomplete Gamma function as our cumulative energy distribution,

$$p(E > E_{\mathrm{th}}) = \int_{E_{\mathrm{th}}}^{\infty}(E/E_{\mathrm{max}})^\gamma \exp(-E/E_{\mathrm{max}})\mathrm{d}E, \tag{14}$$

the derivative of which is often termed the 'Schechter' function. This eliminates numerical artefacts in the analysis of H_0 that can arise due to the infinitely sharp cutoff in the power-law at $E > E_{\mathrm{max}}$.

Although Li et al. (2021) find a minimum burst energy for FRB 20121102, our analysis in J22a showed no evidence of a minimum value of burst energy for the FRB population as a whole, so we set the value of $E_{\mathrm{min}} = 10^{30}$ erg, which is several orders of magnitude below the minimum burst energy of any FRB detected.

Individual FRBs show detailed structure in both the time and frequency domain (Pleunis et al. 2021b), which in the case of repeaters is also highly time-variable (Hessels et al. 2019). As we have discussed in J22a, this introduces ambiguities in modelling their spectral properties. We choose to use the 'rate interpretation' for FRB spectral behaviour, where FRBs are narrow in bandwidth, and have a frequency dependent rate ($\Phi(\nu) \propto \nu^{\alpha}$). This provides an equally good description of FRB properties to the more usual 'spectral index' interpretation in which FRBs have fluences that scale with frequency, and it is computationally much faster to implement.

2.2.3 *Scattering*

The FRB width model used in J22a modelled the total width distribution of FRBs (i.e. including intrinsic width w_i and scattering w_s) as a lognormal with mean $\log \mu_w[\mathrm{ms}] = 1.70$ and $\log \sigma_w = 0.73$. This was based on the fit to observe CRAFT/FE (CRAFT Fly's Eye) and Parkes/Mb (Parkes multibeam) FRBs from Arcus et al. (2021), and accounted for observational biases.

Since all the FRBs used in J22a were detected at $\sim$1.3 GHz, this model was perfectly appropriate. However, when incorporating lower-frequency observations, i.e. the CRAFT/ICS 900 MHz observations used here, it becomes important to separate out the contribution of scattering w_s, which scales approximately as $w_s \sim \nu^{-4}$ (Bhat et al. 2004; Day et al. 2020), and can dominate the FRB width distribution at low frequencies.

The best measure of the scattering distribution of FRBs comes from the CHIME catalogue (CHIME/FRB Collaboration et al. 2021). Using real-time injected bursts to estimate the effect of observational biases, these authors find that the true scattering time distribution at 600 MHz, τ_{600}, follows an approximate lognormal distribution with $\log \mu_s[\mathrm{ms}] = 0.7$ and $\log \sigma_s = 1.72$. We therefore use this result, and scale μ_s as

$$\log \mu_s(\nu) = 0.7 - 4(\log \nu_{\mathrm{obs}}\,\mathrm{MHz} - \log 600\,\mathrm{MHz}). \quad (15)$$

Thus our model for the total effective width w_{eff} of FRBs becomes the quadrature sum of the intrinsic width w_{int}, scattered width w_{scat}, DM smearing width w_{DM}, and sampling time w_{samp}, i.e.

$$w_{\mathrm{eff}} = \sqrt{w_{\mathrm{int}}^2 + w_{\mathrm{scat}}^2 + w_{\mathrm{DM}}^2 + w_{\mathrm{samp}}^2}. \quad (16)$$

From Fig. 1, the measured and bias-corrected width distributions found by CHIME (CHIME/FRB Collaboration et al. 2021) are broadly consistent with the measurements of ASKAP and Parkes (Qiu et al. 2020; Arcus et al. 2021, J22a), but narrower than the bias-corrected values (James et al. 2022a). This is an interesting result in-and-of itself, and assuming it is not due to some difference in the fitting methods, it may imply some frequency-dependent aspect of the FRB emission mechanism, or an unknown selection effect. It is also in contrast to the results of Gajjar et al. (2018), who find that the intrinsic width of bursts from FRB 20211102 decreases with increasing frequency. For our purposes however, we simply retain the previous bias-corrected width distribution from J22a, and add the contribution from scattering according to (15) and the parameters found by CHIME/FRB Collaboration et al. (2021).

3 EXPLORING THE MODEL DEPENDENCIES ON H_0

In this section, we consider examples of the forward model to gain intuition on the constraints for H_0 imposed by the observations as well as key model degeneracies. In the following, we assume

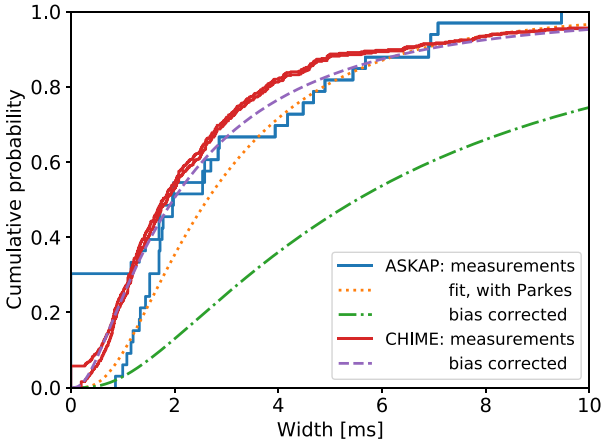

Figure 1. FRB width cumulative distributions. Shown are measurements from ASKAP (Qiu et al. 2020) and CHIME (CHIME/FRB Collaboration et al. 2021) with upper and lower lines calculated by assuming FRBs with upper limits have widths equal to zero and the limit value, respectively. Also shown is a fit to data from ASKAP and Parkes (Arcus et al. 2021), and estimates of the bias-corrected (intrinsic) width distributions (J22a). The ASKAP and Parkes data have not had the effects of scattering removed. Note that we use the total FRB widths, which are twice the reported Gaussian standard deviations.

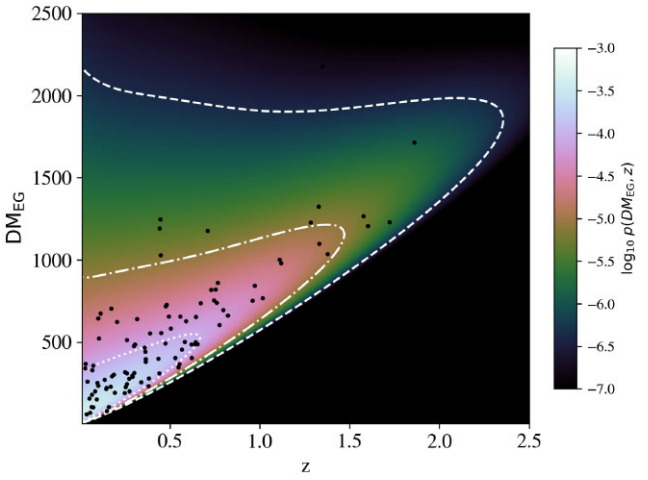

Figure 2. The colour image describes $P(z, \mathrm{DM})$ for the forthcoming CRACO survey on the ASKAP telescope for a fiducial set of model parameters (Table 1). Overplotted are white contours enclosing 50 per cent (dotted), 90 per cent (dash–dotted) and 99 per cent (dashed) of the probability. The black dots are a Monte Carlo realization of the PDF for a random draw of 100 FRBs (Table 6).

properties for future FRB surveys on the ASKAP telescope, using the CRAFT COherent upgrade (CRACO) system. Its characteristics follow the ICS (mid) survey performed on ASKAP by the CRAFT project but with approximately 4.4 times greater sensitivity due to the anticipated coherent addition of 24 antennas (as opposed to the incoherent addition of typically 25), and a slightly reduced bandwidth (from 336 MHz to 288 MHz).

Fig. 2 shows the $P(z, \mathrm{DM})$ probability distribution function (PDF) for this CRACO survey and a fiducial set of model parameters (Table 1) informed by J22a. Overplotted is a Monte Carlo realization of 100 random FRBs drawn from the 2D PDF. These are, as expected, located primarily within the 90 per cent contour in PDF. This Monte

Table 1. Fiducial set of model parameters. Parameters labelled with a $*$ are re-fit as part of this work.

Parameter	Fiducial Value	Unit	Description
$\log_{10}\mu_s$	0.7	ms	Mean of $\log_{10}$-scattering distribution at 600 MHz
$\log_{10}\sigma_s$	1.9	ms	Standard deviation of $\log_{10}$-scattering distribution at 600 MHz
μ_w	1.70267	ms	$\log_{10}$ mean of intrinsic width distribution in ms
σ_w	0.899148	ms	$\log_{10}$ sigma of intrinsic width distribution in ms
$\mathrm{DM_{ISM}}$	NE2001	pc cm^{-3}	DM for the Milky Way interstellar medium
$\mathrm{DM_{halo}}$	50	pc cm^{-3}	DM for the Galactic halo
n^*_{sfr}	0.73		Scaling of FRB rate density with star-formation rate
H^*_0	67.66	km s^{-1} Mpc^{-1}	Hubble's constant
Ω_Λ	0.68885		Dark energy / cosmological constant (in current epoch)
Ω_m	0.30966		Matter density in current epoch
Ω_b	0.04897		Baryon density in current epoch
$\Omega_b h^2$	0.02242		Baryon density weighted by h^2_{100}
μ^*_{host}	2.18		$\log_{10}$ mean of DM host contribution in pc cm^{-3}
σ^*_{host}	0.48		$\log_{10}$ sigma of DM host contribution in pc cm^{-3}
$f_d(z=0)$	0.844		Fraction of baryons that are diffuse and ionized at $z=0$
F	0.32		F parameter in $\mathrm{DM_{cosmic}}$ PDF for the Cosmic web
$\log_{10} E_{\mathrm{min}}$	30	erg	$\log_{10}$ of minimum FRB energy
$\log_{10} E^*_{\mathrm{max}}$	41.4	erg	$\log_{10}$ of maximum FRB energy
α^*	0.65		Power-law index of frequency dependent FRB rate, $R \sim \nu^\alpha$
γ^*	-1.01		Slope of luminosity distribution function

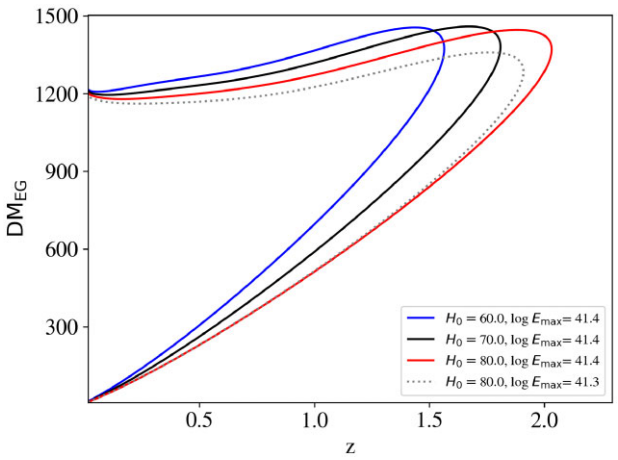

Figure 3. The coloured curves are the 95 per cent contours in the $P(z, \mathrm{DM})$ space for the fiducial CRACO model (Table 1), but with H_0 varying from 60 km s^{-1} Mpc^{-1} (blue) to 80 km s^{-1} Mpc^{-1} (red). As H_0 increases, the contours tilt towards lower $\mathrm{DM_{EG}}$ values due to the ${H_0}^{-1}$ dependence of $\langle \mathrm{DM_{cosmic}} \rangle$ (equation 9). They also extend to higher z because higher H_0 implies a physically smaller universe, i.e. one can observe an FRB with given energy to higher z. This effect, however, is partially degenerate with the energetics of the FRB population as described by the dotted line (a model with lower E_{max}).

Carlo sample is analysed in Section 6 to perform a forecast on the future sensitivity of FRB surveys to H_0.

The $P(z, \mathrm{DM})$ PDF is highly asymmetric with a long tail to large $\mathrm{DM_{EG}}$ values. This asymmetry is driven by the predicted tails in $\mathrm{DM_{cosmic}}$ due to the Poisson nature of cosmic structure (e.g. large $\mathrm{DM_{cosmic}}$ values from galaxy clusters) and the adopted lognormal PDF for $\mathrm{DM_{host}}$. At the highest $\mathrm{DM_{EG}}$ values (>1500 pc cm^{-3}), $P(z, \mathrm{DM})$ tends towards *lower* redshift. This counter-intuitive effect is due to the reduction in SNR by DM-smearing of the signal combined with simple cosmological dimming (Connor 2019, J22a).

Now we consider differences in $P(z, \mathrm{DM})$ due to variations in H_0. Fig. 3 shows the 95 per cent contours in the $P(z, \mathrm{DM})$ plane for a range of H_0 values and two choices of E_{max}. The results may at first seem counter-intuitive. In particular, the models with higher H_0 lean toward *lower* $\mathrm{DM_{EG}}$ values in the $P(z, \mathrm{DM})$ plane even though $\mathrm{DM_{cosmic}} \propto \Omega_b\, h$. This occurs because we have held $\Omega_b\, h^2$ fixed (see Section 2.1) such that increasing H_0 decreases $\Omega_b\, h$ proportionally and therefore $\mathrm{DM_{cosmic}}$ (equation 9) and therefore $\mathrm{DM_{EG}}$. Because the tail to high $\mathrm{DM_{EG}}$ includes attributes of the host ($\mathrm{DM_{host}}$) and the distribution of baryons with the Universe's cosmic web (parameterized by F Macquart et al. 2020), the greatest constraining power on H_0 is from the lower boundary of the contours. This is evident in Fig. 2 where one notes the sharpness of $P(z, \mathrm{DM})$ along the lower edge of the PDF contours.

Another important behaviour seen in Fig. 3 is that the contours 'rotate' within the plane as H_0 varies. All of the other model parameters that significantly affect $\mathrm{DM_{EG}}$ (e.g. those influencing $\mathrm{DM_{host}}$) tend to rigidly shift and/or widen the contours parallel to $\mathrm{DM_{EG}}$. Therefore, there is significant constraining power in the data for H_0 without high degeneracy.

The other notable effect of increasing H_0 is that the contours extend to higher redshift. With all other cosmological parameters fixed (except Ω_b), a universe with higher H_0 is 'smaller'. Surveys with a given flux sensitivity can therefore observe FRBs to higher redshift. This secondary effect, however, is partially degenerate with the FRB luminosity function and especially E_{max}. Fig. 3 shows an additional contour with $H_0 = 80$ km s^{-1} Mpc^{-1} and an E_{max} value 20 per cent lower than the fiducial value. Lowering E_{max} reduces the redshift extent of the $H_0 = 80$ km s^{-1} Mpc^{-1} to be similar to that with a higher E_{max} and $H_0 = 70$ km s^{-1} Mpc^{-1}, although the contours remain offset. This also suggests some sensitivity to the functional form of the luminosity function of (14). We further investigate correlations between H_0 and E_{max} when fitting to data in Section 5.3.

This coupling of H_0 and E_{max} manifests in the other primary FRB observable: s. Put another way to the extent that energetics of the FRB phenomenon are invariant with redshift the analysis is effectively a standard candle. We illustrate the model dependence in Fig. 4, which shows the PDF of $P(z, \mathrm{SNR})$ for several choices of H_0 and E_{max}. There is a strong H_0 dependence on the predicted distribution for s as a function of redshift, but the variance is nearly degenerate with E_{max}, e.g. decreasing H_0 by 10 km s^{-1} Mpc^{-1} is nearly equivalent to

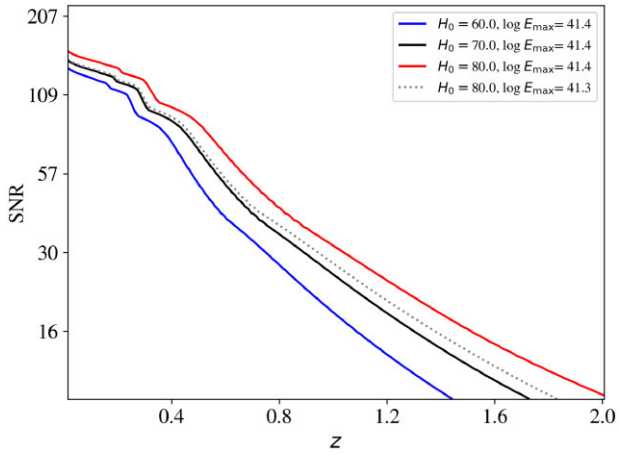

Figure 4. Similar to Fig. 3 except the curves are contours in the $P(z, \mathrm{SNR})$ space (95 per cent of the events are expected to occur below the lines). While the models indicate significant H_0 dependence, these are more nearly degenerate with E_{max} than the results in the $P(z, \mathrm{DM})$ space, e.g, compare the solid black curve with the dotted curve which have significantly differing H_0 and E_{max}.

lowering E_{max} by 0.1 dex (compare the black solid and dotted curves in Fig. 4).

4 OBSERVATIONAL SAMPLE

The FRBs analysed here mainly draw from the same samples of J22a and we refer the reader to that manuscript for full details. Briefly, the three samples used are FRBs detected by the Murriyang (Parkes) Multibeam system (Parkes/Mb; e.g. Staveley-Smith et al. 1996; Keane et al. 2018), ASKAP when observing in Fly's Eye mode (CRAFT/FE; Bannister et al. 2017), and ASKAP when observing in incoherent sum mode (CRAFT/ICS; Bannister et al. 2019, Shannon et al. (in prep.)). Here, we describe updates to this data set, and the methods used to address bias in the data.

Our criteria aim to be inclusive in our data selection in order to overcome the limitations from the small number of localized FRBs. The studies presented in Appendix A suggest that any systematic effects of doing so will be small compared to the statistical error due to small sample size. We expect to revise these criteria when more data become available. See J22a for a discussion of observational biases against high-DM FRBs.

4.1 New localized FRBs

Since the publication of J22a, the CRAFT survey has continued to observe commensally in incoherent sum mode. While observations are still ongoing, we include all FRBs detected up to Dec 31$^{\mathrm{st}}$ 2021. This adds 14 new FRBs to our sample. Their relevant properties are listed in Table 2, while their detailed properties will be given in several works currently in preparation (Deller et al. (in prep.); Shannon et al. (in prep.), Gordon et al., in prep.).

4.2 Addition of FRBs with higher $\mathrm{DM_{ISM}}$

In J22a, only FRBs with $\mathrm{DM_{ISM}} < 100\,\mathrm{pc\,cm^{-3}}$ were included in the analysis. This is because higher values of $\mathrm{DM_{ISM}}$ degrade sensitivity to FRBs, and it is too computationally expensive to calculate sensitivity for each individual FRB. Rather, the simulation uses the mean value of $\mathrm{DM_{ISM}}$ for the sample to calculate this observation bias, while using individual values of $\mathrm{DM_{ISM}}$ to calculate $\mathrm{DM_{EG}}$ for the purposes of likelihood evaluation. This criterion previously rejected eight FRBs from Parkes/Mb, and two FRBs from CRAFT/FE. We show in Appendix A2 that this criterion can be relaxed somewhat, and we now include all previously excluded FRBs. This includes FRB 20010621, which we consider has sufficient excess DM beyond the estimated $\mathrm{DM_{ISM}}$ to be classified as an (extragalactic) FRB. These are listed in Table 3. In the future, when larger numbers of localized FRBs reduce statistical errors, the very small bias due to this approximation could become relevant, and this criterion may have to be revisited.

4.3 Extension to other frequency ranges

ASKAP/CRAFT observations in ICS mode are predominantly fully commensal. This means that FRBs may be detected in any of the four ASKAP observing bands, covering 600–1800 MHz (Hotan et al. 2021). Within each band, the precise choice of which 336 1 MHz frequency channels are available to the CRAFT system also varies on a per-observation basis. Typically however, observations have clustered around two main frequency ranges near 900 MHz and 1.3 GHz with a few further observations near 1.6 GHz. We label these ranges CRAFT/ICS 900 MHz, CRAFT/ICS 1.3 GHz, and CRAFT/ICS 1.6 GHz, respectively. We therefore calculate $P(N_{\mathrm{FRB}})$, the probability of detecting a total of N_{FRB} FRBs, and $P(z, \mathrm{DM}, \mathrm{SNR})$, separately for each of these three frequency ranges, and treat these as independent surveys with N_{FRB} equal to 8, 13, and 1 FRBs, respectively. For computational simplicity, as per J22a within each survey we average the sensitivity over several observation-to-observation differences, such as the number of summed antennas (typically 25), observation frequency, beam configuration, system temperature, and time resolution, as well as $\mathrm{DM_{ISM}}$ as discussed above (however, $\mathrm{DM_{EG}}$ is calculated individually for each FRB).

The extension to frequencies beyond the nominal 1.3 GHz addressed by J22a also requires considering the effects of scattering separately from the intrinsic FRB width, as discussed in Section 2.2.3. It does however allow the inclusion of FRB 20191001, which was excluded from J22a as being the only FRB at the time of analysis to be discovered in CRAFT/ICS observations outside the 1.3 GHz band.

4.4 Consideration of host galaxy probability

The redshifts associated with each localized FRB are derived from observations of the host galaxy, which necessarily requires a firm association of the FRB with that galaxy. The Probabilistic Association of Transients to their Hosts (PATH; Aggarwal et al. 2021) gives a method to calculate posterior probabilities $P(O|x)$ of any given host galaxy association, while accounting for FRB localization uncertainties. In the original analysis, seven of nine CRAFT/ICS FRB host galaxies associations were found with $P(O|x) > 95$ per cent.

Bhandari et al. (2022) has performed an updated PATH analysis of three localized CRAFT FRBs, and reported a posterior probability $P(O|x)$ for the host association exceeding 90 per cent in each case. In Shannon et al. (in prep.), we argue that one should modify the standard PATH priors introduced by Aggarwal et al. (2021), which increases the $P(O|x)$ values for these and all previous FRBs from CRAFT/ICS. Thus all localized FRBs in our sample have posterior values of $P(O|x)$ of 90 per cent or greater, as listed in Table 2.

Table 2. ASKAP incoherent sum FRBs used in this analysis. Given is the FRB name, SNR-maximising DM, DM_{ISM} estimated using the NE2001 model of Cordes & Lazio (2002), central frequency of observation ν, measured signal-to-noise ratio SNR, redshift z, posterior probability of host associations $P(O|x)$, and original reference. Where redshifts are not given, this is because (a): no voltage data were dumped, preventing radio localization; (b) optical follow-up observations are not yet complete; (c) substantial Galactic extinction has challenged follow-up optical observations; (d) the host galaxy appears too distant to accurately measure a redshift.

Name	DM (pc cm^{-3})	DM_{ISM} (pc cm^{-3})	ν (MHz)	SNR	z	$P(O\|x)$	Ref.
			CRAFT/ICS 900 MHz				
20191001	506.92	44.2	919.5	62.0	0.23	0.973	Bhandari et al. (2020)
20200430	380.1	27.0	864.5	16.0	0.161	1.000	Heintz et al. (2020)
20200906	577.8	35.9	864.5	19.2	0.36879	1.000	Bhandari et al. (2022)
20210807	251.9	121.2	920.5	47.1	0.12927	0.957	Deller et al. (in prep.)
20200627	294.0	40.0	920.5	11.0	(a)	n/a	Shannon et al. (in prep.)
20210320	384.8	42.2	864.5	15.3	0.2797	0.999	–
20210809	651.5	190.1	920.5	16.8	(a)	n/a	–
20211203	636.2	63.4	920.5	14.2	(b)	n/a	–
			CRAFT/ICS 1.3 GHz				
20180924	362.4	40.5	1297.5	21.1	0.3214	0.999	Bannister et al. (2019)
20181112	589.0	40.2	1297.5	19.3	0.4755	0.927	Prochaska et al. (2019b)
20190102	364.5	57.3	1271.5	14	0.291	1.000	Macquart et al. (2020)
20190608	339.5	37.2	1271.5	16.1	0.1178	1.000	–
20190611.2	322.2	57.6	1271.5	9.3	0.378	0.980	–
20190711	594.6	56.6	1271.5	23.8	0.522	0.999	–
20190714	504.7	38.5	1271.5	10.7	0.209	1.000	Heintz et al. (2020)
20191228	297.5	32.9	1271.5	22.9	0.243	1.000	Bhandari et al. (2022)
20210117	730	34.4	1271.5	27.1	0.2145	0.999	Bhandari et al. (in prep.)
20210214	398.3	31.9	1271.5	11.6	(a)	n/a	Shannon et al. (in prep.)
20210407	1785.3	154	1271.5	19.1	(c)	n/a	–
20210912	1234.5	30.9	1271.5	31.7	(d)	n/a	–
20211127	234.83	42.5	1271.5	37.9	0.0469	0.998	Deller et al. (in prep.)
			CRAFT/ICS 1.6 GHz				–
20211212	206	27.1	1632.5	12.8	0.0715	0.998	Deller et al. (in prep.)

Table 3. Properties of CRAFT/FE and Parkes/Mb FRBs previously excluded due to their relatively high DM_{ISM}, which are now included in this analysis. Given is the original FRB designation; measured total DM and DM_{ISM} estimated by the NE2001 model (Cordes & Lazio 2002) in pc cm^{-3}, and ratio of measured to threshold SNR.

FRB	DM	DM_{ISM}	SNR	Ref.
		Parkes/Mb		
20150610	1593.9	104	18	Bhandari et al. (2018)
20151206	1909.8	239	10	–
20171209	1457.4	329	40	Osłowski et al. (2019)
20180714	1467.92	254	22	–
20150418	776.2	164	39	Keane et al. (2016)
20010125	790	105	17	Burke-Spolaor & Bannister (2014)
20010621	745	502	16.3	Keane et al. (2011)
20150215	1105.6	405	19	Petroff et al. (2017)
		CRAFT/FE		
20180315	479.0	100.8	10.5	Macquart et al. (2019)
20180430	264.1	169	28.2	Qiu et al. (2019)

4.5 CRAFT/ICS FRBs with no hosts

The results and forecasts presented thus far have implicitly assumed that we have observed a complete and unbiased sample from the FRB surveys. We recognize, however, that there is no perfect FRB survey nor related follow-up efforts (e.g. to obtain the FRB redshift). Of the FRBs included in Table 2, six have no identified host. There are many potential reasons for this (numbers are for the current sample in Table 2):

(i) the buffered data necessary for localization was not available for technical reasons (3 FRBs);

(ii) the FRB host is obscured either by proximity to bright stars, or by high levels of dust extinction in the Milky Way (1 FRB);

(iii) the FRB host has not been observed yet, due to being too close to the Sun, or simply because the FRB is so recent that observations have not yet been completed (1 FRB);

(iv) the FRB host cannot be identified amongst several candidate galaxies (no FRBs yet);

(v) the FRB host is too distant or faint to be detected with ground-based follow-up observations (1 FRB).

It is critical therefore that these effects do not introduce biases into our analysis.

Of the above, reasons (i), (ii), and (iii) are clearly uncorrelated with the properties of the FRBs themselves so that while missing these FRBs reduces our statistical power using P(DM) rather than $P(z,$ DM) introduces no bias. Reason (iv) is a function of both the radio localization accuracy, and the number and properties of galaxies in the FRB field. While more distant FRBs are on-average dimmer (Shannon et al. 2018), and thus will have a greater statistical error on their localization, the correlation between SNR and z is relatively weak; furthermore, the localization accuracy of CRAFT/ICS FRBs is typically dominated by systematics in FRB image alignment (Day et al. 2021), which are uncorrelated with FRB properties. However, since angular diameter distance is increasing over the redshift range of observed CRAFT/ICS FRBs, a constant angular resolution will result in a more-difficult host galaxy identification with increasing z, making it more likely to preferentially reject FRBs from high redshifts. Furthermore, one may not be able to obtain a sufficiently high-quality spectrum of the galaxy to confidently measure its redshift. Reason (v) is clearly correlated with redshift: an FRB follow-up observation probing to a limiting r-band magnitude of 22 might be insufficient to detect a $0.1\,L^*$ galaxy beyond $z = 1$ or a $0.01\,L^*$ galaxy beyond a redshift of 0.1 (Eftekhari & Berger 2017).

We deal with these biases here by choosing a maximum extra-galactic dispersion measure, $\mathrm{DM}_{\mathrm{EG}}^{\mathrm{max}} = 1000\,\mathrm{pc\,cm^{-3}}$, beyond which detected FRBs are classified as unlocalized regardless of whether or not their host has been identified. To avoid bias in redshift, it is critical that this criterion is independent of z; however, these FRBs must be included in the calculation of P(DM) to avoid bias in that parameter. Our localizations are sufficiently certain that we are not currently affected by reason (iv). FRBs which are unlocalized for any other reason are also included in the calculation of P(DM) rejecting these would not introduce a bias, but would reduce the statistical power of the sample. We show in Appendix A3, how this procedure allows an unbiased measure of H_0. In total, six CRAFT/ICS FRBs are treated this way – see Table 2.

4.6 Observation time and low-SNR bias

The question of observational bias against low-SNR FRBs has a long history (Macquart & Ekers 2018a; James et al. 2019b). An analysis of the measured SNR of CRAFT/ICS FRBs however reveals that the majority of FRBs with SNR $\lesssim 15$ have been undetected, resulting in a total FRB rate which is approximately half that expected (Shannon et al., in prep.). Under the simplifying assumption of a Euclidean slope of (N_{FRB} > SNR) $\propto \mathrm{SNR}^{-1.5}$, we expect that for every FRB detected with SNR ≥ 15, 1.15 are detected in the range $9 \leq \mathrm{SNR} \leq 15$, where $\mathrm{SNR_{th}} = 9$ is the nominal CRAFT/ICS detection threshold. However, CRAFT/ICS have detected 16 FRBs with SNR ≥ 15, and only 6 with SNR ≤ 15, when 18.4 might be expected. Some of the missing low-SNR FRBs can be attributed to periods of high RFI ($\lesssim$10 per cent of the searches), where the detection threshold had to be raised as high as $\mathrm{SNR_{th}} = 14$; however, in most cases, this loss remains unexplained. We note that there is neither evidence for such a bias in CRAFT/FE data, nor does there appear to be a correlation between missing FRBs and properties such as DM or frequency, although our ability to probe this is affected by low-sample numbers.

The assumption of a 50 per cent loss of FRBs due to a bias against low-SNR events is also backed up by calculations of the absolute CRAFT/ICS 1.3 GHz FRB rate (Shannon et al., in prep), which was not available in time for use in J22a. The expected rate of CRAFT/ICS 1.3 GHz FRBs is relatively model-independent, since the frequency range is almost identical to, and the sensitivity lies between CRAFT/FE and Parkes/Mb observations. This reveals a detection rate which is approximately half that expected, which is consistent with the low-SNR bias described above.

We account for this issue therefore by taking the absolute observation time of CRAFT/ICS observations measured by Shannon et al. (in prep), and divide by half to represent the 50 per cent loss of detection efficiency. Importantly, the measured FRB rate of CRAFT/ICS 900 MHz and CRAFT/ICS 1.6 GHz observations allows us to have better statistical inference on the frequency-dependent rate parameter α, which aside from a prior based on the results of Macquart et al. (2019) was largely unconstrained in J22a. In Appendix A1, we demonstrate that missing FRBs in this small SNR range does not cause any significant bias in the determination of H_0, so we retain the threshold of $\mathrm{SNR_{th}} = 9.0$.

Table 4. Parameters and their values (in linear increments from min to max values) at which the joint likelihood $P(z,$ DM, SNR) was evaluated. $\log_{10} E_{\mathrm{min}}$ was fixed at 10^{30} erg.

Parameter	Min	Max	Increment
H_0	55	101	2
$\log_{10} E_{\mathrm{max}}$	40.5	42.5	0.1
α	0	2	0.5
γ	−1.5	−0.5	0.1
n	0	3	0.25
μ_{host}	1.5	2.6	0.1
σ_{host}	0.3	1.1	0.1

5 RESULTS

We evaluate $P(N_{\mathrm{FRB}})$ for each survey, and $P(z,$ DM, SNR) for each FRB in that survey over a seven-dimensional cube of parameters with values given in Table 4. Posterior probabilities are calculated from the resulting product over all FRBs and surveys using uniform priors over the simulated parameter ranges, while confidence intervals on those parameters are constructed using the prescription of Feldman & Cousins (1998). Our results are given below. The best-fitting z–DM distribution for ASKAP FRBs is shown in Fig. 5.

5.1 H_0

Our posterior probability distribution for H_0 is given in Fig. 6. We simulate only up to $H_0 = 103\,\mathrm{km\,s^{-1}\,Mpc^{-1}}$: in the range above $80\,\mathrm{km\,s^{-1}\,Mpc^{-1}}$, we find the probability to be decreasing as a log-normal to better than 1 per cent relative accuracy, so we save significant compute time and extrapolate results to $H_0 = 130\,\mathrm{km\,s^{-1}\,Mpc^{-1}}$. Our best-fitting value is $H_0 = 73^{+12}_{-8}\,\mathrm{km\,s^{-1}\,Mpc^{-1}}$. While this agrees with values of H_0 derived from near-Universe measures, it is also consistent within $1\,\sigma$ of indirect values derived from e.g. the CMB (Abdalla et al. 2022).

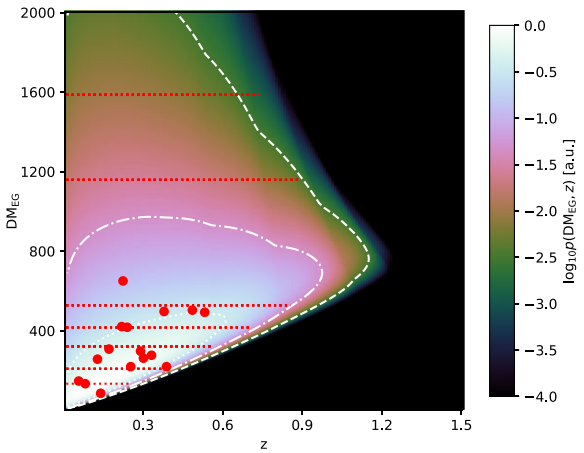

Figure 5. The z–DM distribution of FRBs (shading) using best-fitting model parameters summed over the CRAFT/ICS 900 MHz, CRAFT/ICS 1.3 GHz, and CRAFT/ICS 1.6 GHz samples. Also shown are FRBs with (red solid circles) and without (red dashed lines) host galaxy redshifts. The latter are drawn at their estimated values of $\mathrm{DM_{EG}}$ out to z_{99}, i.e. encompassing 99 per cent of their likelihood in $P(z|\mathrm{DM})$ for their $\mathrm{DM_{EG}}$ values. White contours of dotted, dash–dotted, and dashed lines encompass 50, 90, and 99 per cent of the probability density of $P(z, \mathrm{DM})$, respectively.

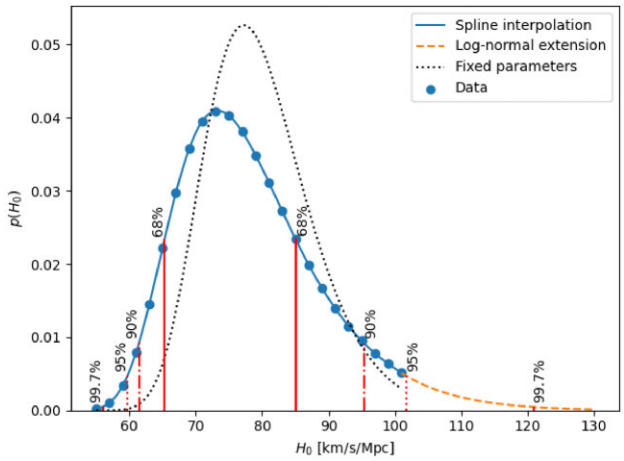

Figure 6. Posterior probability on H_0 using cubic splines (blue solid curve) fitted to data points (circles) using uniform priors over the simulated range, and extrapolated to higher values of H_0 using a lognormal fit (orange dashed curve). Confidence intervals are also shown (vertical red lines). The posterior probability when fixing all other parameters to their best-fitting values is also shown (grey dotted curve).

Our constraint on H_0 is not symmetric – we derive a relatively sharp lower boundary with looser constraints on large values of H_0. This is the result of what we term 'the cliff effect', whereby large excess DMs above the mean can be induced by intersection with galaxy haloes or host galaxy contributions, but even voids contribute a minimum $\mathrm{DM_{cosmic}}$. Thus, probability distribution $P(z|\mathrm{DM})$ has a sharp lower cut-off, or 'cliff'. Low values of H_0 thus imply a higher minimum DM as a function of z, and when this minimum is contradicted by even a single measured FRB, those values of H_0 can be excluded. Higher values of H_0 however do not suffer such a large penalty due to the long tail of the $P(\mathrm{DM}|z)$ distribution.

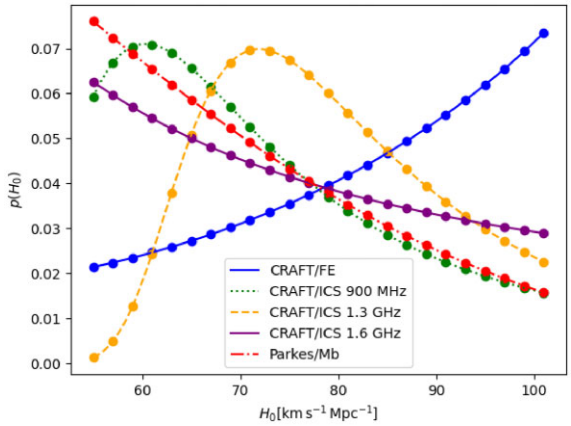

Figure 7. Posterior probability on H_0 using cubic splines (solid curves) fitted to data points (squares) using uniform priors over the simulated range for each of the five FRB surveys used in this work.

Fig. 6 also shows the constraint on H_0, we would derive if all other FRB parameters are fixed to their best-fitting values. This demonstrates the importance of performing a multiparameter fit and marginalising over nuisance parameters. Even in the case that the fixed values of FRB parameters are well-guessed (i.e. at the best-fitting values used here), ignoring the confounding effects of uncertainties in these parameters none the less leads to a biased and artificially too-precise estimate of H_0.

It is also interesting to examine the constraints on H_0 from each FRB survey individually. This is shown in Fig. 7. The two surveys with large numbers of localized FRBs, CRAFT/ICS 900 MHz and CRAFT/ICS 1.3 GHz, provide the dominant constraints, as expected. That CRAFT/ICS 1.3 GHz is better fit by a higher value of H_0 is due to the cliff effect and FRB 20190102, which has a very low DM of 322.2 pc cm^{-3} for its redshift of 0.378. The single localized FRB of CRAFT/ICS 1.6 GHz provides a comparable amount of information to CRAFT/FE and Parkes/Mb with 26 and 28 FRBs each illustrates the importance of localized FRB samples when constraining H_0.

5.2 Constraints on other parameters

Besides constraints on H_0, our addition of new localized FRBs yields greater statistical power to constrain the other fitted parameters, $\log_{10}E_{\mathrm{max}}$, α, γ, n_{sfr}, μ_{host}, and σ_{host}, while also accounting for the confounding effect of allowing H_0 to vary. However, since our constraint on H_0 using FRB data only is significantly less than that of other measurements, we apply a prior on H_0, which is flat between the best-fitting CMB and SN1A values (67.4 and 74.03 km s^{-1} Mpc^{-1}), and falls away as a Gaussian on the lower/upper regions with the respective uncertainties of those measurements (0.5 and 1.42 km s^{-1} Mpc^{-1}).

Posterior probability distributions on these parameters are shown in Fig. 8, while confidence limits on all parameters are reported in Table 5. For comparison, we also show results with no prior on H_0, which give worse constraints, and also results when assuming H_0 is fixed to either the value of 67.4 obtained by Planck Collaboration VI (2020) or 74.03 from Riess et al. (2021), representing the improvement in accuracy should H_0 be known exactly.

We confirm the result of James et al. (2022b) that the FRB population exhibits cosmological source evolution consistent with

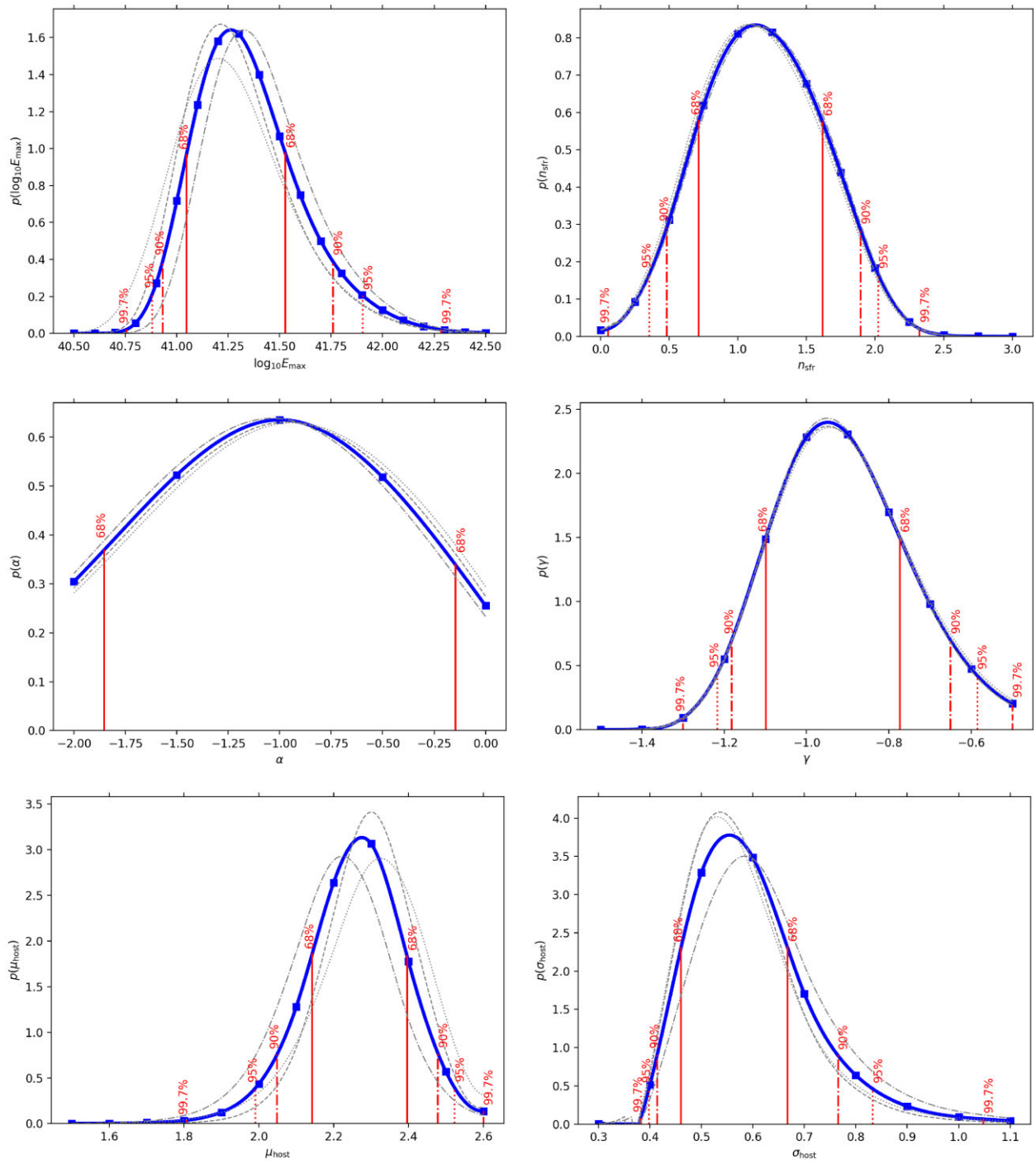

Figure 8. Posterior probabilities on the six other estimated parameters using a prior for H_0 based on CMB and SN1a results (blue curves; see text). Also shown are posterior probabilities with no prior on H_0 (grey dotted curves) and with H_0 fixed to 67 km s^{-1} Mpc^{-1} (grey dash-dotted curves) and 73 km s^{-1} Mpc^{-1} (grey dashed curves).

the star-formation rate, excluding no source evolution ($n = 0$) at $3\,\sigma$. This is in-line with the expectations from models predicting a close association between star-forming activity and FRB progenitors in particular young magnetar models (e.g. Metzger, Berger & Margalit 2017), but does not exclude that a fraction of FRBs could arise from channels with a significant (∼Gyr) characteristic delay from star formation, such as mergers. It does exclude that the majority of FRB progenitors have a cosmologically significant delay with respect to star formation. We observe that other results in the literature that analyse FRB population evolution (e.g. Cao, Yu & Zhou 2018; Locatelli et al. 2019; Arcus et al. 2021; Bhattacharyya et al. 2022) tend to assume a 1–1 z–DM (i.e. a purely linear) relationship, and/or fix values of other FRB population parameters, which are assumptions which we do not make.

We also find an increased value of $\mu_{\rm host} = 2.27^{+0.12}_{-0.13}$, i.e. a median host DM of 186^{+59}_{-48} pc cm^{-3} (the corresponding mean DM is

Table 5. Best-fitting parameter values and associated confidence intervals for each fitted parameter. For parameters other than H_0, limits are given for different priors on H_0: the 'standard' prior, covering both early- and local-Universe measurements of H_0 (see text), fixing H_0 to 67.4 km s^{-1} Mpc^{-1} and 74.03 km s^{-1} Mpc^{-1}, and a flat prior between 55 and 101 km s^{-1} Mpc^{-1}. For α, only approximate 68 per cent errors are given (see text).

Parameter	Prior	Best Fit	68 per cent	90 per cent	95 per cent	99.7 per cent
H_0	N/A	73.0	$^{+12}_{-8}$	$^{+22}_{-12}$	$^{+29}_{-13}$	$^{+48}_{-17}$
$\log_{10} E_{\rm max}$	Std	41.26	$^{+0.27}_{-0.22}$	$^{+0.50}_{-0.33}$	$^{+0.64}_{-0.38}$	$^{+1.02}_{-0.51}$
	67.4	41.20	$^{+0.29}_{-0.25}$	$^{+0.52}_{-0.39}$	$^{+0.67}_{-0.45}$	$^{+1.06}_{-0.61}$
	74.03	41.21	$^{+0.26}_{-0.21}$	$^{+0.49}_{-0.32}$	$^{+0.63}_{-0.37}$	$^{+1.03}_{-0.49}$
	Flat	41.33	$^{+0.27}_{-0.22}$	$^{+0.50}_{-0.33}$	$^{+0.63}_{-0.38}$	$^{+0.99}_{-0.50}$
α	Std	-0.99	$^{+0.99}_{-1.01}$		N/A	
	67.4	-0.92	$^{+0.92}_{-1.08}$		N/A	
	74.03	-0.95	$^{+0.95}_{-1.05}$		N/A	
	Flat	-1.03	$^{+1.03}_{-0.97}$		N/A	
γ	Std	-0.95	$^{+0.18}_{-0.15}$	$^{+0.30}_{-0.23}$	$^{+0.36}_{-0.27}$	$^{+0.45}_{-0.36}$
	67.4	-0.94	$^{+0.18}_{-0.15}$	$^{+0.30}_{-0.24}$	$^{+0.37}_{-0.27}$	$^{+0.44}_{-0.36}$
	74.03	-0.95	$^{+0.18}_{-0.15}$	$^{+0.30}_{-0.23}$	$^{+0.37}_{-0.27}$	$^{+0.45}_{-0.36}$
	Flat	-0.95	$^{+0.17}_{-0.15}$	$^{+0.29}_{-0.23}$	$^{+0.36}_{-0.27}$	$^{+0.45}_{-0.35}$
$n_{\rm sfr}$	Std	1.13	$^{+0.49}_{-0.41}$	$^{+0.77}_{-0.65}$	$^{+0.90}_{-0.77}$	$^{+1.19}_{-1.09}$
	67.4	1.08	$^{+0.50}_{-0.41}$	$^{+0.78}_{-0.64}$	$^{+0.92}_{-0.76}$	$^{+1.21}_{-1.05}$
	74.03	1.10	$^{+0.50}_{-0.41}$	$^{+0.78}_{-0.63}$	$^{+0.92}_{-0.75}$	$^{+1.21}_{-1.06}$
	Flat	1.15	$^{+0.49}_{-0.41}$	$^{+0.76}_{-0.66}$	$^{+0.89}_{-0.79}$	$^{+1.18}_{-1.11}$
$\mu_{\rm host}$	Std	2.27	$^{+0.12}_{-0.13}$	$^{+0.21}_{-0.23}$	$^{+0.26}_{-0.28}$	$^{+0.33}_{-0.47}$
	67.4	2.33	$^{+0.13}_{-0.14}$	$^{+0.21}_{-0.25}$	$^{+0.25}_{-0.31}$	$^{+0.27}_{-0.57}$
	74.03	2.30	$^{+0.11}_{-0.12}$	$^{+0.19}_{-0.20}$	$^{+0.24}_{-0.25}$	$^{+0.30}_{-0.40}$
	Flat	2.23	$^{+0.13}_{-0.14}$	$^{+0.22}_{-0.25}$	$^{+0.28}_{-0.31}$	$^{+0.37}_{-0.51}$
$\sigma_{\rm host}$	Std	0.55	$^{+0.12}_{-0.09}$	$^{+0.22}_{-0.13}$	$^{+0.30}_{-0.16}$	$^{+0.51}_{-0.21}$
	67.4	0.53	$^{+0.11}_{-0.08}$	$^{+0.22}_{-0.13}$	$^{+0.29}_{-0.15}$	$^{+0.52}_{-0.20}$
	74.03	0.54	$^{+0.11}_{-0.08}$	$^{+0.20}_{-0.13}$	$^{+0.27}_{-0.15}$	$^{+0.48}_{-0.20}$
	Flat	0.57	$^{+0.13}_{-0.09}$	$^{+0.25}_{-0.14}$	$^{+0.33}_{-0.17}$	$^{+0.51}_{-0.21}$

240 pc cm^{-3}), which is significantly greater than the usually assumed value of 100 pc cm^{-3} found in the literature. This may not reflect entirely upon the actual FRB host galaxy: our fit to $\mu_{\rm host}$ will include any error in our assumed mean value of $\rm DM_{halo} = 50\,pc\,cm^{-3}$, and some component of $\sigma_{\rm host}$ will include scatter about that mean, and also errors in $\rm DM_{ISM}$. However, since our used values of $\rm DM_{halo} = 50\,pc\,cm^{-3}$, and NE2001 for $\rm DM_{ISM}$ are typical of the literature; it does suggest that the average work on FRBs is underestimating some combination of $\rm DM_{host}$, $\rm DM_{ISM}$, and/or $\rm DM_{halo}$, and thus over-estimating $\rm DM_{cosmic}$. Other results, such as the excess DM of $\sim$900 pc cm^{-3} observed for FRB20190520B by Niu et al. (2022), and the suggestion of correlation between the locations of CHIME FRBs and large-scale structure at an excess DM of $\sim$400 pc cm^{-3} (Rafiei-Ravandi et al. 2021) support this conclusion.

The slope of the intrinsic luminosity function γ is found to be $-0.95^{+0.18}_{-0.15}$, consistent with the observed high-energy slope of the luminosity functions of known repeating FRBs, e.g. $\gamma = -0.85 \pm 0.3$ (Li et al. 2021), $-0.88 > \gamma > -1.29$ (Jahns et al. 2022), and $\gamma = -1.04 \pm 0.02$ (Hewitt et al. 2022) for FRB 20121102A. This is consistent with, though not sufficient proof of, apparently once-off FRBs being simply the high-energy tails of intrinsically repeating objects.

The posterior distribution of α drops only to approximately half its peak value over our simulated range ($-2 \leq \alpha \leq 0$), suggesting an uncertainty of ± 0.85. Thus we should consider that we have used a uniform top-hat prior on α. None the less, unlike J22a, we have significant discrimination power on α. Our best-fitting value of $\alpha = -1.0 \pm 0.85$ is consistent with the result of Macquart et al. (2019), who find $\alpha = -1.5^{+0.2}_{-0.3}$ under the assumption that each FRB is characteristically broad-band with a spectral slope, which (as argued in J22a) should be revised to $\alpha = -0.65^{+0.2}_{-0.3}$ under the 'rate approximation' used here. This disfavours the results of CHIME/FRB Collaboration et al. (2021) and Farah et al. (2019), which do not include the effects of observational bias that there is no increase of the FRB rate at decreasing frequency.

We conclude this section by noting that none of the above results are strongly dependent on our choice of prior on H_0 (none; based on existing literature; or fixed) with the greatest effect being on $E_{\rm max}$ and $\mu_{\rm host}$.

5.3 Correlations with other parameters

We illustrate the correlations between parameters in Fig. 9. We only show results for correlations between H_0 and other parameters, since J22a has already analysed other correlations. For each plot, we hold all other parameters constant at their best-fitting values and plot the conditional probability $p(H_0|X)$ for each parameter X. From Fig. 9, H_0 is correlated with all modelled parameters, emphasizing the importance of jointly fitting them.

Some correlations are readily understood. As $\mu_{\rm host}$ increases, the implied $\rm DM_{cosmic}$ decreases favouring smaller distances being travelled by the FRB, and hence larger values of H_0. The strong negative correlation of H_0 with low values of $E_{\rm max}$ is because smaller values of $E_{\rm max}$ require that distances to localized FRBs decrease to allow these FRBs to be detectable, which requires larger values of H_0. However, once $E_{\rm max}$ is sufficiently large ($\log_{10} E_{\rm max} > 41.5$), there is essentially no correlation. The sharp increase of H_0 for $\log_{10} E_{\rm max} > 42.5$, and for $n_{\rm sfr} > 2.5$, is driven by the Parkes/Mb sample, where for these extreme values of $\log_{10} E_{\rm max}$ and $n_{\rm sfr}$, a large H_0 is required to reduce the DM of the otherwise very large number of distant FRBs that Parkes/Mb would be able to detect.

As γ increases, more FRBs are generated near $E_{\rm max}$, and are thus visible from larger distances (higher z), while the effect of the experimental bias against high DMs is reduced (higher DM for a given z). It turns out for this data set that the latter effect is more important, and a positive correlation arises since increasing H_0 reduces the expected DM.

That $\sigma_{\rm host}$ is anti-correlated with H_0, particularly for low values, can be understood via the cliff effect. Reducing $\sigma_{\rm host}$ narrows the distribution of $\rm DM_{EG}$ about the Macquart relation. The reduced extent of the high-DM tail still allows for excess-DM FRBs above the relation, albeit with reduced probability however, a small reduction in $\sigma_{\rm host}$ massively decreases the likelihood of observing FRBs below the Macquart relation. To model this requires increasing H_0, since that pulls the Macquart relation downward, as shown in Fig. 3.

For most values of $n_{\rm sfr}$ there is a very slight anti-correlation with H_0, since increasing both parameters can act to increase the fraction of high-redshift FRBs. However, for $n_{\rm sfr} \gtrsim 2.5$, there is a strong positive correlation. This is largely driven by $P(N_{\rm FRB})$, where increasing H_0 decreases the volume in which very large numbers of FRBs would otherwise be predicted.

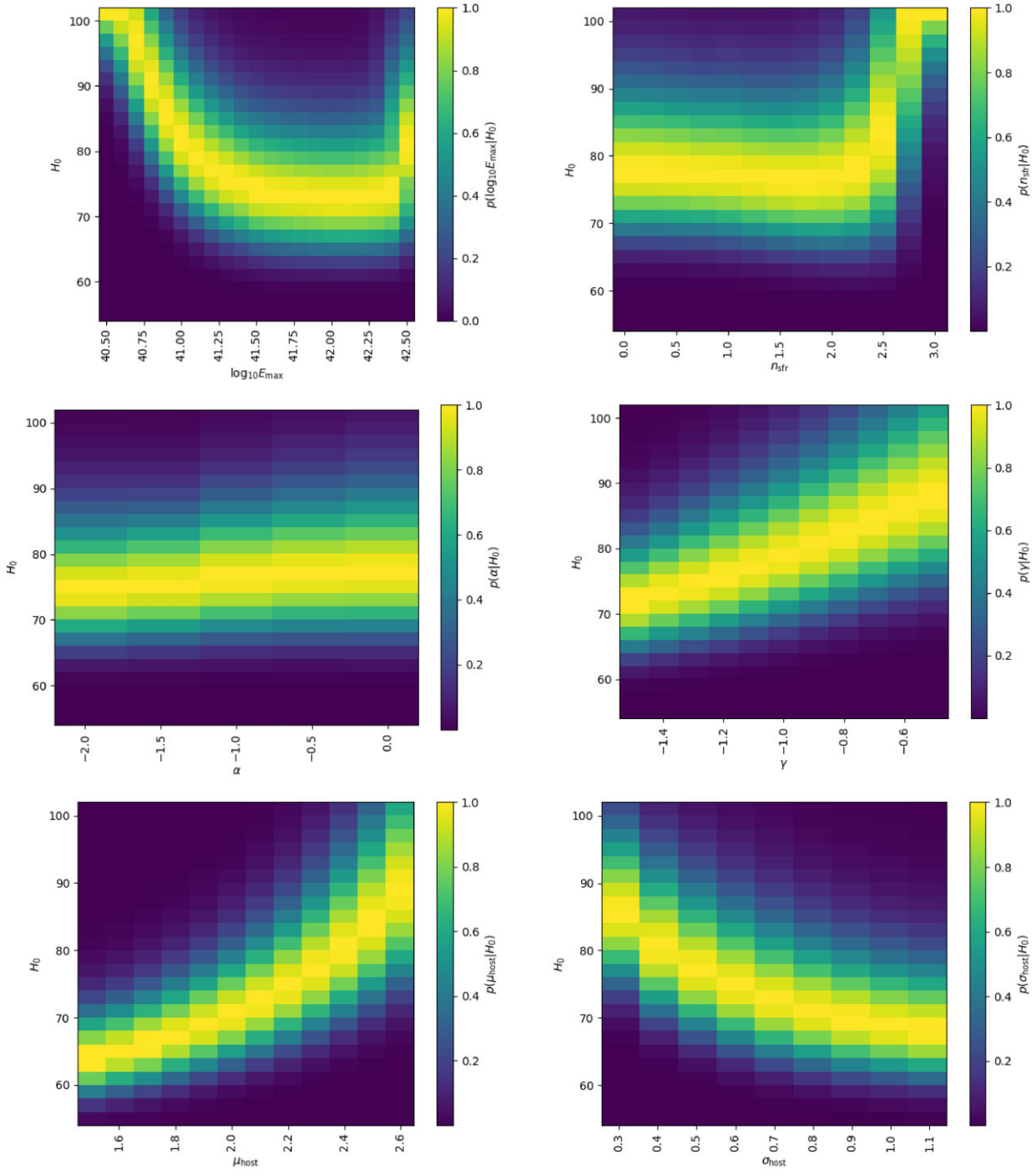

Figure 9. Conditional posterior probabilities on H_0 when allowing only single parameters to vary from their best-fitting values. These plots describe degeneracies in the results between H_0 and the other model parameters.

The slight positive correlation between the spectral rate parameter α and H_0 is a combination of multiple minor effects, the sum of which has little impact on the determination of H_0. The influence of α will be constrained in the future by including FRB data from a wider range of frequencies.

6 FORECASTS – CRACO MONTE CARLO

Our limit on H_0 using the 16 localized and 60 unlocalized FRBs is not sufficiently constraining to discriminate between direct measurements from the local Universe and indirect measurements from the early Universe. However, in the near future, several experiments promise to greatly increase the number of localized FRBs. In particular, CRACO aims to implement a fully coherent image-plane FRB search during 2022.[2] The searches will be undertaken commensally with all other ASKAP observations.

We model CRACO by assuming $N_{\rm ant} = 24$ of ASKAP's 36 antennas are coherently added over a $\Delta\nu = 288$ MHz bandwidth.

[2]https://dataportal.arc.gov.au/NCGP/Web/Grant/Grant/LE210100107

Scaling the 22 Jy ms detection threshold to a 1 ms burst of the $\Delta\nu = 336$ MHz Fly's Eye survey (James et al. 2019a) by $N_{\rm ant}^{-1}(\Delta\nu)^{-0.5}$ gives an estimated detection threshold of $F_{\rm th} = 0.99$ Jy ms. Assuming a Euclidean dependence of the FRB rate on sensitivity (i.e. $R \propto F_{\rm th}^{1.5}$), the Fly's Eye rate of 20 FRBs in 1427 antenna days of observing predicts a 100-fold rate increase to 1.5 FRBs d^{-1} at high Galactic latitudes. This is then reduced by telescope down-time RFI time spent observing in the Galactic plane, and other efficiency losses in both radio observing and optical follow-up observations to identify host galaxies. Here, we use 100 FRBs to nominally represent the first year's worth of CRACO observations. These FRBs are listed in Table 6, since they may be useful for other CRACO-related predictions, e.g. for gauging the requirements of optical follow-up observations.

We draw parameters s, DM, and z randomly from the simulated distribution of $P(z, \mathrm{DM}, \mathrm{SNR})$ assuming Monte Carlo truth values of $H_0 = 67.66$ km s^{-1} Mpc^{-1} and best-fit FRB population parameters from James et al. (2022b). These FRBs are plotted in Fig. 2 and listed in Table 6. We repeat our calculation of $P(z, \mathrm{DM}, \mathrm{SNR})$ over the multidimensional grid of parameters given in Table 4, albeit limiting this to a more constrained range of H_0. The resulting Bayesian posterior probability distribution on H_0 is given in Fig. 10.

For this particular FRB sample, we find $H_0 = 66.28^{+2.6}_{-2.3}$ km s^{-1} Mpc^{-1} consistent with the MC truth value of 67.66 km s^{-1} Mpc^{-1}. Importantly, the statistical uncertainty of $\sim$2.45 km s^{-1} Mpc^{-1}, which includes the increased variance when fitting for FRB population parameters would provide 2.5σ evidence to discriminate between the $\sim$6 km s^{-1} Mpc^{-1} difference in estimates of H_0 (Abdalla et al. 2022). Assuming only statistical errors to achieve 5σ discriminatory power would require 400 localized FRBs.

This suggests that near-future FRB observations, and perhaps only a single year's worth of 100 per cent efficient observations with the CRACO upgrade on ASKAP will be able to help resolve the current discrepancy in the two measurements of H_0. It also motivates a careful treatment of potential systematic errors, both in the FRB sample used, and in the cosmological and FRB population model. We discuss such errors in Section 7.2.

7 DISCUSSION

7.1 Comparison to other estimates of H_0 with FRBs

Both Wu, Zhang & Wang (2022) (Wu22) and Hagstotz, Reischke & Lilow (2022) (HS22) use measurements of FRBs to constrain H_0, finding $H_0 = 68.8^{+5.0}_{-4.3}$ km s^{-1} Mpc^{-1} and $H_0 = 62.3 \pm 9.1$ km s^{-1} Mpc^{-1}, respectively. These values are compatible at the 1σ level with our result of 73^{+12}_{-8} km s^{-1} Mpc^{-1}, however, it is still useful to analyse differences in the methods, especially given that common data was used.

Wu22 and HS22 use 18 and 9 localized FRBs, respectively in both cases including a sub-set of the bursts used in this analysis, and those from other instruments. These include repeating FRBs which have been localized purely because they are repeaters, which presents a biased distribution of the underlying population (Gardenier et al. 2019), although the effect of this bias is difficult to determine. Furthermore, no study accounts for observational biases against high DMs, which will systematically increase H_0 by assuming the artificially low measured mean DMs reflect the true underlying distribution.

Both Wu22 and HS22 model DM contributions according to (1)–(3) with Wu22 in particular using very similar functional

Table 6. Monte Carlo FRBs generated for the (in development) CRACO system on ASKAP (see Section 6).

DM	SNR (pc cm^{-3})	z
186.7	15.9	0.15
1179.5	26.0	1.321
438.5	20.2	0.062
315.3	17.9	0.089
833.1	10.5	0.949
595.3	32.8	0.25
313.4	16.8	0.37
568.5	13.1	0.629
143.5	11.0	0.026
743.4	12.6	0.812
941.9	10.0	0.755
460.5	10.7	0.355
1271.8	12.1	0.432
1308.6	15.7	1.273
567.9	12.4	0.608
410.5	84.7	0.057
391.1	117.3	0.251
1287.8	9.7	1.592
634.8	15.9	0.378
383.0	15.6	0.176
372.7	16.2	0.167
237.3	13.3	0.041
478.8	27.0	0.354
835.0	51.2	0.735
282.6	10.6	0.263
151.4	223.4	0.046
819.9	13.1	0.75
162.3	17.3	0.138
371.1	25.0	0.282
357.4	16.3	0.262
331.8	40.2	0.085
557.5	88.5	0.289
818.5	9.8	0.66
1257.6	22.4	0.699
1116.3	11.6	1.367
2259.2	12.3	1.338
307.9	22.6	0.243
1311.1	24.4	1.712
848.2	11.6	1.006
1060.6	10.6	1.108
785.5	10.0	0.164
484.9	11.7	0.52
481.2	9.6	0.424
484.7	14.9	0.61
260.6	12.9	0.054
393.8	12.7	0.291
273.7	22.7	0.182
534.4	21.0	0.556
703.6	10.8	0.195
335.9	18.5	0.329
898.1	32.2	0.718
582.2	13.8	0.571
636.2	23.1	0.441
735.7	27.7	0.482
1405.0	11.4	1.318
1083.0	19.3	1.101
709.4	12.4	0.58
1794.1	14.9	1.849
736.2	11.0	0.546
808.6	33.4	0.472
352.0	16.0	0.126

Table 6 – *continued*

DM	SNR (pc cm^{-3})	z
447.5	38.3	0.543
1346.2	12.3	1.567
428.3	12.3	0.537
421.8	28.0	0.018
602.3	16.3	0.093
1110.1	94.0	0.439
303.5	10.8	0.137
799.7	18.8	0.465
309.6	30.0	0.159
3446.6	25.6	0.08
721.5	25.8	0.306
296.3	21.4	0.134
573.2	19.6	0.464
184.5	11.4	0.063
580.0	15.6	0.632
754.0	9.6	0.103
391.9	11.2	0.43
282.0	21.7	0.073
548.7	25.8	0.35
449.7	12.6	0.019
187.9	40.8	0.052
522.1	11.8	0.353
233.3	85.5	0.081
923.9	9.9	0.961
568.1	15.9	0.295
1327.1	18.6	0.437
901.0	39.8	0.744
776.9	14.5	0.786
359.8	46.4	0.372
733.7	18.7	0.633
685.6	9.8	0.765
568.9	14.8	0.644
398.7	23.3	0.239
664.2	15.8	0.495
326.6	14.2	0.251
726.0	23.7	0.089
342.1	48.2	0.029
376.5	47.9	0.279
271.9	18.9	0.237

forms. HS22 however uses Gaussian distributions in linear space to model both DM_{host} and DM_{cosmic}, given that they are symmetric about the mean. They neither include the high-DM tail, nor the relatively sharp lower limit to DM for a given redshift expected for DM_{EG}.

Importantly, both Wu22 and HS22 allow for an uncertainty in DM_{local}, using $\sigma_{MW} = 30\,pc\,cm^{-3}$ with Wu22 also allowing DM_{halo} to vary in the range 50–80 pc cm^{-3}. Allowing for such uncertainties is an important next step in our model due to the influence of the cliff effect.

Neither Wu22 nor HS22 however allow assumed values for other parameters in their model to vary, and H_0 is particularly sensitive to the assumed value of μ_{host} (see Fig. 9). HS22 assumes $\mu_{host} = 100\,pc\,cm^{-3}$, while Wu22 use a model for μ_{host} based on the simulations of Zhang et al. (2020) with μ_{host} increasing with z, and varying according to the class of FRB host galaxy (see discussion below). However, all values of μ_{host} are lower than our best-fitting median value of $10^{\mu_{host}} = 186\,pc\,cm^{-3}$. Since their assumed values are low, their assumed DM_{IGM} will be increased, which we attribute as being primarily responsible for the lower H_0 values estimated by these authors.

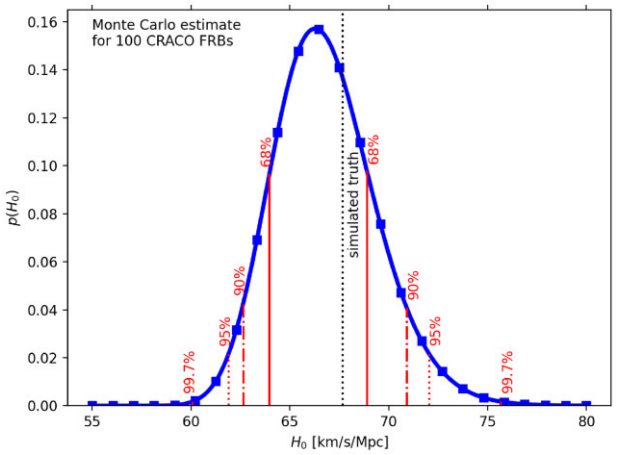

Figure 10. Posterior distribution on H_0 calculated from our Monte Carlo sample of 100 simulated FRBs that would be detected by the ASKAP CRACO upgrade (blue). Also shown are confidence intervals (red; labelled), and the simulated true value (black vertical line). Results with a uniform and Gaussian prior on α are indistinguishable.

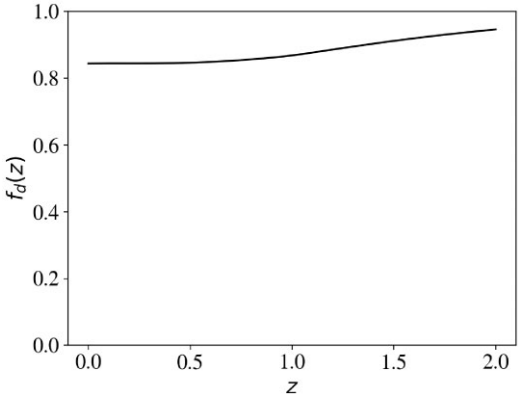

Figure 11. Modelled redshift evolution of the fraction of baryons that are diffused and ionized $f_d(z)$ calculated according to Macquart et al. (2020) using code from Prochaska et al. (2019a).

7.2 Sources of uncertainty and bias

In this analysis, we have not allowed for uncertainties in the cosmological parameters $f_d(z)$, $\Omega_b h^2$, and the feedback parameter F. Of these, the current experimental uncertainty in $\Omega_b h^2$ is $\mathcal{O} \sim 0.5$ per cent (Mossa et al. 2020a), and negligible compared to errors in the current calculation. In the future, we will need to marginalize over this uncertainty.

Our adopted estimate for the fraction of baryons that are diffuse and ionized, $f_d(z)$ follows the methodology introduced in Prochaska et al. (2019a), and discussed in further detail in Macquart et al. (2020). The approach uses the estimated mass density of baryons in dense (i.e. neutral) gas and compact objects (stars, stellar remnants) from observations and stellar population modelling. For the present-day, one recovers $f_d(z = 0) = 0.844$ using the Planck Collaboration VI (2020) parameters to estimate the total mass density in baryons. The redshift evolution of $f_d(z)$ is plotted in Fig. 11. Regarding uncertainty in $f_d(z)$, the stellar mass estimate dominates primarily

through our imprecise knowledge of the stellar initial mass function (IMF). If we assume a 30 per cent uncertainty in the stellar mass density (and associated remnants), this translates to a 4 per cent uncertainty in $f_d(z=0)$. As the statistical power of the FRB sample grows, this systematic error in $f_d(z)$ will rise in importance for H_0 analysis. It is possible, however, that upcoming experiments including weak-lensing surveys will reduce the IMF uncertainties. We also emphasize that at higher redshifts, f_d increases as the masses of galaxies decreases. For example, a 30 per cent error in the stellar mass contribution at $z = 1$ leads to a $\approx$2.5 per cent error in $f_d(z = 1)$. In this respect, by including FRBs at $z > 1$ one can partially alleviate the uncertainty in $f_d(z)$.

The feedback parameter F acts to smear the distribution of $\mathrm{DM_{IGM}}$ about the mean with smaller values representing a larger 'feedback' effect that reduces the gas content of galactic haloes, and hence a less clumpy Universe with a less smeared distribution of $\mathrm{DM_{IGM}}$ (Cen & Ostriker 2006). To first order, the influence of F is similar to the smearing of $\mathrm{DM_{host}}$ by σ_{host}. Since both contribute to variance in $\mathrm{DM_{EG}}$, and we fit σ_{host} to this, first-order uncertainties in F are absorbed into σ_{host}. However, variance in $\mathrm{DM_{EG}}$ due to $\mathrm{DM_{host}}$ is modelled as decreasing with z, while the absolute variance in $\mathrm{DM_{IGM}}$ (due to F) increases with z. However, for future FRB samples, particularly those including localizations at $z \gtrsim 1$, these terms should be separated, and F explicitly fitted. For now, we note that σ_{host} and H_0 do show significant (anti-)correlation, and thus potentially errors in our (somewhat arbitrarily) adopted value of $F = 0.32$ could influence our measurement of H_0, although we expect that the main effect of such an error is to shift the fitted value of σ_{host}.

Related to this, we have used a fixed functional form for $\mathrm{DM_{host}}$, which while allowing for the reduced DM due to redshift, does not allow for evolution of the host galaxy properties themselves. Indeed, our adopted lognormal distribution is not theoretically motivated, but rather is a qualitatively good description of the expected high-DM tail of $\mathrm{DM_{host}}$. An improved model, including redshift evolution will likely require combining FRB host galaxy studies (e.g. Bhandari et al. 2022) to derive empirical correlations similar to treatments of Hubble residuals with supernovae (e.g. Phillips 1993). For instance, Zhang et al. (2020) find a cosmic evolution of $\mu_{\mathrm{host}} = C_{\mathrm{DM}}(1+z)^{\alpha_{\mathrm{DM}}}$ with constant $33 \leq C_{\mathrm{DM}} \leq 96\,\mathrm{pc\,cm^{-3}}$ and $0.83 \leq \alpha_{\mathrm{DM}} \leq 1.08$, depending on galaxy type. Thus, when including the $(1+z)^{-1}$ redshift penalty to $\mathrm{DM_{host}}$, the observed distribution of $\mathrm{DM_{host}}$ should remain almost constant with redshift. Since C_{DM} varies with galaxy type however, so that the distribution of galaxy types, and thus presumably FRB host galaxies and thus μ_{host} will also vary with redshift. We suggest this topic for future investigations.

'$\mathrm{DM_{host}}$' represents all contributions to DM that come from the FRB occurring in a non-random part of the Universe, and thus includes the local cosmic structure (e.g. filament) halo, and interstellar medium of the host, and the immediate environment of the progenitor. Improvements in modelling should target all these aspects. One path forward is to use optical observations of the FRB host galaxy environment and intervening matter (Lee et al. 2022b), combined with properties such as the rotation measure and scattering of the FRB itself (Cordes, Ocker & Chatterjee 2022) to constrain these values on a per-FRB basis.

Finally, we note that our models for the FRB luminosity function, and spectral behaviour are relatively simplistic, the true behaviour is likely more complicated. These are discussed in more detail in J22a, and both can be investigated through near-Universe observations of FRBs.

7.3 Comparison with other methods

It is interesting to compare and contrast FRBs with other probes of H_0 in the local Universe. The traditional method of using Type Ia Supernovae (SNIa) relies on these being calibratable standard candles, using the cosmological distance ladder and in particular Cepheid variables (e.g. Riess et al. 2021, and references therein). This is certainly not the case for FRBs, which show a vast range of luminosity (Spitler et al. 2014; Shannon et al. 2018). However, using early Universe constraints on $\Omega_b h^2$ allows FRB DM to effectively become a 'standard candle', directly relating the value of DM to distance via the Macquart relation. This means however that FRB measures of H_0 in the local Universe will not be fully independent of early Universe cosmological fits, but can none the less be used to identify an inconsistent cosmology.

Both methods suffer from potential biases due to a changing nature of host galaxies with redshift, and concerns regarding dust extinction biases in SNIa (see e.g. Sullivan et al. 2003) are analogous to FRB detection biases against high DMs induced by FRB host galaxies. As discussed above, FRBs are sensitive to local Universe contributions to DM, which are less well-known than Galactic extinction effects on SN1a. Thus in many ways, FRB determination of H_0 is qualitatively similar to, but independent of, measures derived from SNIa, making them a perfect method for determining if the current Hubble tension is a result of systematic errors in the distance ladder, or a sign of new cosmology beyond ΛCDM.

Current limits on H_0 from FRBs are much less accurate than those from SNIa with statistical errors of $^{+12}_{-8}\,\mathrm{km\,s^{-1}\,Mpc^{-1}}$ compared to $\pm 1.01\,\mathrm{km\,s^{-1}\,Mpc^{-1}}$ for SN1a (Riess et al. 2021). New experiments promise to dramatically increase the rate of both samples – the Legacy Survey of Space and Time (LSST) to be performed by the Rubin Observatory is expected to detect 400 000 Type Ia supernovae (Ivezić et al. 2019), while CRACO, DSA2000 (Hallinan, Ravi & Walter 2022), and CHORD (Vanderlinde et al. 2019) expect to increase the number of localized FRBs to the tens of thousands, although making use of this sample will require significant investment on optical telescopes to obtain host redshifts.

Gravitational wave (GW) detections also promise to constrain H_0 (Schutz 1986). Since the intrinsic signal strength is precisely predicted from general relativity, there is essentially no calibration uncertainty. The challenge however lies in the event rate of localizable GW signals, which is very low with so-far only a single event yielding an uncertainty of $70.3^{+5.3}_{-5.0}\,\mathrm{km\,s^{-1}\,Mpc^{-1}}$ (Hotokezaka et al. 2019). There are also only moderate improvements expected in the near future (Abbott et al. 2020): a 1.8 per cent precision on H_0 would require 50–100 binary neutron star (BNS) mergers with host galaxies, or 15 which also have afterglow information constraining their inclination angle (Hotokezaka et al. 2019). The expected rate of BNS detection during the upcoming fourth observing run ('O4') of the LIGO–Virgo–KAGRA GW detectors[3] at $7.7^{+11.9}_{-5.7}\,\mathrm{yr^{-1}}$ is too uncertain to make hard predictions about the time required to reach these numbers (Colombo et al. 2022). The $\sim$78 per cent fraction of these events that will produce a kilonova (and hence redshift via host galaxy identification), and $\sim$10 per cent fraction that will produce a detectable jet constraining their inclination angle, must also be considered (Colombo et al. 2022).

Therefore, provided that the systematic errors discussed in Section 7.2 can be reduced, FRBs will be a valuable cosmological probe,

[3] https://www.ligo.caltech.edu/news/ligo20211115

should be at least as precise as GW-based approaches, and have the potential to approach SN1a in precision.

8 CONCLUSIONS

Using a sample of 16 localized and 60 unlocalized FRBs, we have fitted the observed values of SNR, z, and DM for each FRB, and the number of FRBs observed by each survey, using a Bayesian approach. We use the methodology of James et al. (2022a), which includes the biasing effects of telescope beamshape and the FRB width, and models the FRB luminosity function, source evolution, and properties of the FRB population and their host galaxies. We have updated the method to allow H_0 to vary while adjusting Ω_b according to precise constraints on $\Omega_b h^2$ from the CMB. We find a best-fitting value of 73^{+12}_{-8} km s^{-1} Mpc^{-1}, consistent with both direct and indirect measures of H_0 (Abdalla et al. 2022), and other estimates using FRBs (Hagstotz et al. 2022; Wu et al. 2022). This estimate was obtained with uniform priors over the entire range of $\mu_{\rm host}$, $\sigma_{\rm host}$, $\log_{10}E_{\rm max}$, γ, and $n_{\rm sfr}$ where the likelihood is non-vanishing, and the plausible range of $-2 \leq \alpha \leq 0$ allowed by other studies.

We discuss systematic differences in the different methodologies for inferring H_0 from FRB samples, and we attribute the lower values of H_0 found by those studies to be primarily due to their low assumed values of $\rm DM_{host}$, which we fit finding a median host contribution of 186^{+59}_{-48} pc cm^{-3} (from an assumed Galactic halo contribution of $\rm DM_{halo} = 50\,pc\,cm^{-3}$).

The addition of new data confirms the previous result of James et al. (2022b) that the FRB population evolves with redshift in a manner consistent with the star-formation rate, and excludes no source evolution at $3\,\sigma$. This is consistent with young magnetar scenarios, and the presence of FRBs near spiral arms (Mannings et al. 2021), although we do not specifically exclude older progenitors. We have also constrained the frequency dependence of the FRB rate, albeit weakly, finding that $R_{\rm FRB} \propto \nu^{-1\,\pm\,0.85}$. Our estimated slope of the cumulative luminosity function is $\gamma = -0.95^{+0.18}_{-0.15}$, slightly flatter than previous estimates, and consistent with values derived from individual repeating FRBs.

We have used Monte Carlo simulations to predict that 100 localized FRBs from the first year of operation of the CRACO system of ASKAP will be able to constrain H_0 with a statistical uncertainty of $\approx\pm 2.45$ km s^{-1} Mpc^{-1}, giving significant power to discriminate between different existing estimates. This motivates further work to address systematic uncertainties in our modelling, in particular to constrain or fit the fraction of cosmic baryons in diffuse ionized gas, and the contribution of the Milky Way halo to DM.

ACKNOWLEDGEMENTS

Authors J.X.P., A.C.G., and N.T. as members of the Fast and Fortunate for FRB Follow-up team acknowledge support from NSF grants AST-1911140 and AST-1910471. This research was partially supported by the Australian Government through the Australian Research Council's Discovery Projects funding scheme (project DP210102103). R.M.S. acknowledges support through Australian Research Council Future Fellowship FT190100155. S.B. is supported by a Dutch Research Council (NWO) Veni Fellowship (VI.Veni.212.058). The authors thank Evan Keane for comments on the manuscript.

This research has made use of the NASA/IPAC Extragalactic Database (NED), which is operated by the Jet Propulsion Laboratory, California Institute of Technology under contract with the National Aeronautics and Space Administration. This research made use of Python libraries MATPLOTLIB (Hunter 2007), NUMPY (van der Walt, Colbert & Varoquaux 2011), and SCIPY (Virtanen et al. 2020). This work was performed on the gSTAR national facility at Swinburne University of Technology. gSTAR is funded by Swinburne and the Australian Government's Education Investment Fund. This work was supported by resources provided by the Pawsey Supercomputing Centre with funding from the Australian Government and the Government of Western Australia.

The Australian SKA Pathfinder is part of the Australia Telescope National Facility (https://ror.org/05qajvd42) which is managed by CSIRO. Operation of ASKAP is funded by the Australian Government with support from the National Collaborative Research Infrastructure Strategy. ASKAP uses the resources of the Pawsey Supercomputing Centre. Establishment of ASKAP, the Murchison Radio-astronomy Observatory, and the Pawsey Supercomputing Centre are initiatives of the Australian Government with support from the Government of Western Australia and the Science and Industry Endowment Fund. We acknowledge the Wajarri Yamatji people as the traditional owners of the Observatory site.

This research is based on observations collected at the European Southern Observatory under ESO programmes 0102.A-0450(A), 0103.A-0101(A), 0103.A-0101(B), 105.204W.001, 105.204W.002, and 105.204W.003.

DATA AVAILABILITY

The code used in this study is available from GitHub (Prochaska et al. 2019a; James, Prochaska & Ghosh 2021), which also includes the input FRB data. The calculated values of $P(N_{\rm FRB})$ and $P(z, \rm DM, SNR)$ for each dataset take up several GB, and a download link is available upon request to the authors.

REFERENCES

Abbott B. P. et al., 2020, Living Rev. Relativ., 23, 3
Abdalla E. et al., 2022, JHEAp, 34, 49
Aggarwal K., Budavári T., Deller A. T., Eftekhari T., James C. W., Prochaska J. X., Tendulkar S. P., 2021, ApJ, 911, 95
Arcus W. R., Macquart J. P., Sammons M. W., James C. W., Ekers R. D., 2021, MNRAS, 501, 5319
Aver E., Berg D. A., Olive K. A., Pogge R. W., Salzer J. J., Skillman E. D., 2021, J. Cosmology Astropart. Phys., 2021, 027
Bannister K. W. et al., 2017, ApJ, 841, L12
Bannister K. W. et al., 2019, Science, 365, 565
Bhandari S. et al., 2018, MNRAS, 475, 1427
Bhandari S. et al., 2020, ApJ, 901, L20
Bhandari S. et al., 2022, AJ, 163, 69
Bhat N. D. R., Cordes J. M., Camilo F., Nice D. J., Lorimer D. R., 2004, ApJ, 605, 759
Bhattacharyya S., Tiwari H., Bharadwaj S., Majumdar S., 2022, MNRAS, 513, L1
Burke-Spolaor S., Bannister K. W., 2014, ApJ, 792, 19
Caleb M., Flynn C., Stappers B. W., 2019, MNRAS, 485, 2281
Cao X.-F., Yu Y.-W., Zhou X., 2018, ApJ, 858, 89
Cen R., Ostriker J. P., 2006, ApJ, 650, 560
Chime/Frb Collaboration et al., 2020, Nature, 582, 351
CHIME/FRB Collaboration et al., 2021, ApJS, 257, 59
Colombo A., Salafia O. S., Gabrielli F., Ghirlanda G., Giacomazzo B., Perego A., Colpi M., 2022, ApJ, preprint (arXiv:2204.07592)
Connor L., 2019, MNRAS, 487, 5753
Cooke R. J., Pettini M., Steidel C. C., 2018, ApJ, 855, 102
Cordes J. M., Lazio T. J. W., 2002, preprint (arXiv:astro-ph/0207156)
Cordes J. M., Ocker S. K., Chatterjee S., 2022, ApJ, 931, 88
Day C. K. et al., 2020, MNRAS, 497, 3335

Day C. K., Deller A. T., James C. W., Lenc E., Bhandari S., Shannon R. M., Bannister K. W., 2021, PASA, 38, e050
Eftekhari T., Berger E., 2017, ApJ, 849, 162
Farah W. et al., 2019, MNRAS, 488, 2989
Feldman G. J., Cousins R. D., 1998, Phys. Rev. D, 57, 3873
Freedman W. L. et al., 2001, ApJ, 553, 47
Gajjar V. et al., 2018, ApJ, 863, 2
Gardenier D. W., van Leeuwen J., Connor L., Petroff E., 2019, A&A, 632, A125
Hagstotz S., Reischke R., Lilow R., 2022, MNRAS, 511, 662
Hallinan G., Ravi V., Walter F., 2022, Bulletin of the American Astronomical Society, 54, #409.06
Heintz K. E. et al., 2020, ApJ, 903, 152
Hessels J. W. T. et al., 2019, ApJ, 876, L23
Hewitt D. M. et al., 2022, MNRAS, 515, 3577
Hotan A. W. et al., 2021, PASA, 38, e009
Hotokezaka K., Nakar E., Gottlieb O., Nissanke S., Masuda K., Hallinan G., Mooley K. P., Deller A. T., 2019, Nat. Astron., 3, 940
Hunter J. D., 2007, Comput. Sci. Eng., 9, 90
Inoue S., 2004, MNRAS, 348, 999
Ivezić, Ž. et al., 2019, ApJ, 873, 111
Jahns J. N. et al., 2022, MNRAS, preprint (arXiv:2202.05705)
James C. W. et al., 2019a, PASA, 36, e009
James C. W., Ekers R. D., Macquart J. P., Bannister K. W., Shannon R. M., 2019b, MNRAS, 483, 1342
James C. W., Ekers R. D., Macquart J.-P., Bannister K. W., Shannon R. M., 2019c, MNRAS, 483, 1342
James C. W., Prochaska J. X., Ghosh E. M., 2021, zenodo. Available at: https://zenodo.org/record/5213780#.YRxh5BMzZKA
James C. W., Prochaska J. X., Macquart J. P., North-Hickey F. O., Bannister K. W., Dunning A., 2022a, MNRAS, 509, 4775 (J22a)
James C. W., Prochaska J. X., Macquart J. P., North-Hickey F. O., Bannister K. W., Dunning A., 2022b, MNRAS, 510, L18
Keane E. F., Kramer M., Lyne A. G., Stappers B. W., McLaughlin M. A., 2011, MNRAS, 415, 3065
Keane E. et al., 2016, Nature, 530, 453
Keane E. F. et al., 2018, MNRAS, 473, 116
Keating L. C., Pen U.-L., 2020, MNRAS, 496, L106
Lee K.-G., Ata M., Khrykin I. S., Huang Y., Prochaska J. X., Cooke J., Zhang J., Batten A., 2022a, ApJ, 928, 9
Lee K.-G., Ata M., Khrykin I. S., Huang Y., Prochaska J. X., Cooke J., Zhang J., Batten A., 2022b, ApJ, 928, 9
Lemos T., Gonçalves R. S., Carvalho J. C., Alcaniz J. S., 2022, preprint (arXiv:2205.07926)
Li D. et al., 2021, Nature, 598, 267
Locatelli N., Ronchi M., Ghirlanda G., Ghisellini G., 2019, A&A, 625, A109
Lorimer D. R., Bailes M., McLaughlin M. A., Narkevic D. J., Crawford F., 2007, Science, 318, 777
Macquart J. P. et al., 2020, Nature, 581, 391
Macquart J.-P., Ekers R. D., 2018a, MNRAS, 474, 1900
Macquart J.-P., Ekers R., 2018b, MNRAS, 480, 4211
Macquart J.-P., Johnston S., 2015, MNRAS, 451, 3278
Macquart J.-P., Shannon R. M., Bannister K. W., James C. W., Ekers R. D., Bunton J. D., 2019, ApJ, 872, L19
Madau P., Dickinson M., 2014, ARA&A, 52, 415
Madhavacheril M. S., Battaglia N., Smith K. M., Sievers J. L., 2019, Phys. Rev. D, 100, 103532
Mannings A. G. et al., 2021, ApJ, 917, 75
Masui K. W., Sigurdson K., 2015, Phys. Rev. Lett., 115, 121301
McQuinn M., 2014, ApJ, 780, L33
Metzger B. D., Berger E., Margalit B., 2017, ApJ, 841, 14
Mossa V. et al., 2020a, Nature, 587, 210
Mossa V. et al., 2020b, Nature, 587, 210
Niu C. H. et al., 2022, Nature, 606, 873
Osłowski S. et al., 2019, MNRAS, 488, 868
Petroff E. et al., 2014, ApJL, 789, L26
Petroff E. et al., 2017, MNRAS, 469, 4465
Phillips M. M., 1993, ApJ, 413, L105
Planck Collaboration VI, 2020, A&A, 641, A6
Platts E., Weltman A., Walters A., Tendulkar S. P., Gordin J. E. B., Kandhai S., 2019, Phys. Rep., 821, 1
Platts E., Prochaska J. X., Law C. J., 2020, ApJ, 895, L49
Pleunis Z. et al., 2021a, ApJ, 911, L3
Pleunis Z. et al., 2021b, ApJ, 923, 1
Prochaska J. X., Zheng Y., 2019, MNRAS, 485, 648
Prochaska J. X., Simha S., Law C., Tejos N., Neeleman M., 2019a, Zenodo. Available at: https://zenodo.org/record/3403651#.YRxkcBMzZKA
Prochaska J. X. et al., 2019b, Science, 365, aay0073
Qiu H., Bannister K. W., Shannon R. M., Murphy T., Bhandari S., Agarwal D., Lorimer D. R., Bunton J. D., 2019, MNRAS, 486, 166
Qiu H. et al., 2020, MNRAS, 497, 1382
Rafiei-Ravandi M. et al., 2021, ApJ, 922, 42
Rajwade K. M. et al., 2020, MNRAS, 495, 3551
Riess A. G. et al., 2016, ApJ, 826, 56
Riess A. G. et al., 2021, ApJ, 934, L7
Schutz B. F., 1986, Nature, 323, 310
Shannon R. M. et al., 2018, Nature, 562, 386
Spitler L. G. et al., 2014, ApJ, 790, 101
Spitler L. et al., 2016, Nature, 531, 202
Staveley-Smith L. et al., 1996, PASA, 13, 243
Sullivan M. et al., 2003, MNRAS, 340, 1057
Suyu S. H. et al., 2017, MNRAS, 468, 2590
van der Walt S., Colbert S. C., Varoquaux G., 2011, Comput. Sci. Eng., 13, 22
Vanderlinde K. et al., 2019, The Canadian Hydrogen Observatory and Radio-transient Detector (CHORD). Zenodo. Availableat: https://doi.org/10.5281/zenodo.3765414
Virtanen P. et al., 2020, Nature Methods, 17, 261
Wu Q., Zhang G.-Q., Wang F.-Y., 2022, MNRAS, 515, L1
Zhang G. Q., Yu H., He J. H., Wang F. Y., 2020, ApJ, 900, 170

APPENDIX A: STUDIES OF SYSTEMATIC EFFECTS

In this Appendix, we present several studies of potential systematic effects which, if not properly controlled, could bias our estimates of H_0.

A1 Missing low-SNR FRBs

The question of completeness in FRB surveys has been discussed by several authors (e.g. Bhandari et al. 2018; Macquart & Ekers 2018a; James et al. 2019c). From a simulation perspective, we assume completeness above some signal-to-noise threshold, $\mathrm{SNR_{th}}$, i.e. all FRBs with $\mathrm{SNR_{FRB}} > \mathrm{SNR_{th}}$ are detected. However, practically, this may not be the case. FRBs which pass the threshold are usually required to be either visually inspected, and/or analysed by an algorithm to distinguish these events from RFI. Such an inspection, whether done by human or machine, will be more likely to fail for weak FRBs than for strong ones. This observational bias has been suggested as one reason why the first FRB to be discovered; the 'Lorimer burst' (FRB 20010724; Lorimer et al. 2007) was exceptionally bright, because all the other bursts which had been viewed, but were not so bright, had not been identified (Macquart & Ekers 2018a). It has also been suggested to explain the dearth of Parkes FRBs with SNR < 14, although there is no evidence of such a bias from the CRAFT/FE observations (James et al. 2019b).

For CRAFT/ICS observations, the detection threshold, $\mathrm{SNR_{th}}$, initially had to be set as high as 14σ to reduce the number of false RFI candidates. Subsequently, an improved clustering algorithm, SNOOPY2, was developed to analyse all events satisfying $\mathrm{SNR_{FRB}} > \mathrm{SNR_{th}}$ and reject RFI. This algorithm has been shown to pass all FRBs

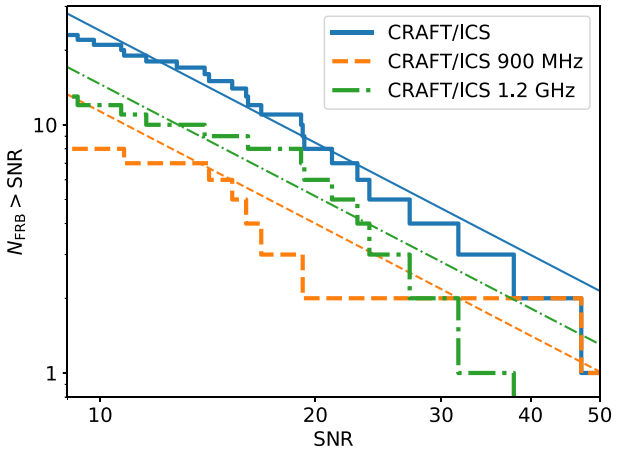

Figure A1. Cumulative event count as a function of FRB SNR for all CRAFT/ICS observations (blue, solid), and separated into CRAFT/ICS 900 MHz (orange, dashed) and CRAFT/ICS 1.3GHz (green, dot–dashed). Only two CRAFT/ICS 1.6 GHz FRBs were detected and are not shown separately. Also shown are fits to a $\mathrm{SNR}^{-1.5}$ power law.

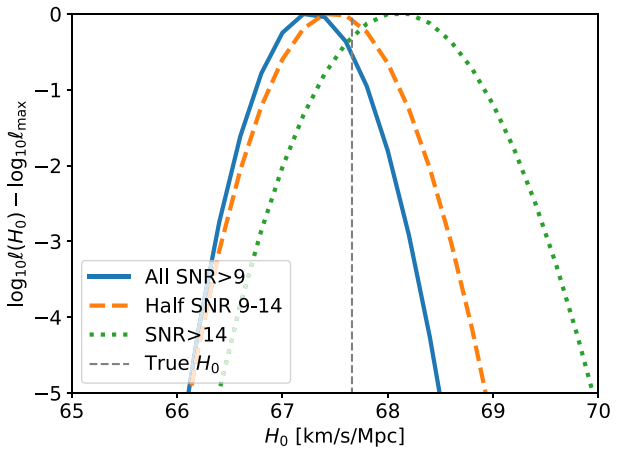

Figure A2. Simulated sensitivity to H_0 of CRAFT/ICS 1.3 GHz observations when using all events with SNR $\geq$ 9, excluding half in the range 9 $\leq$ SNR < 14, and only using events with SNR $\geq$ 14.

detected in ASKAP/FE observations. Furthermore, ASKAP/ICS observations of pulsars have not shown any evidence of behaviour that would reject true FRBs, i.e. all pulsar pulses above the detection threshold are not rejected. Thus CRAFT/ICS observations typically use a threshold of 9σ.

Fig. A1 plots the number of ASKAP FRBs observed above different SNR values. In a Euclidean Universe, this log N–log S curve should have a power-law slope of −1.5. However, for CRAFT/ICS, there is evidence for an inflection point near SNR of 15. While part of this inflection can be explained by early observations with a high $\mathrm{SNR_{th}}$, the threshold had stablized by the time of the 900 MHz observations – and the inflection point is present at both frequency ranges.

The source of this deficit of low-SNR FRBs is unknown. One potential solution is to artificially increase the detection threshold to an SNR of 15, and to discard all FRBs with SNR < 15. Before discarding valuable events however, we first investigate the potential bias of including FRBs in the range 9.5 < SNR < 15.

To do so, we simulate 1000 FRBs from CRAFT/ICS 1.3 GHz using $\mathrm{SNR_{th}} = 9$, and calculate the likelihood $\ell(H_0)$ while holding all other parameters constant. As this is a single survey, $P(N_{\mathrm{FRB}})$ has no contribution, since the population density can always be appropriately scaled. The result is shown in Fig. A2. We then repeat the calculation by randomly removing half of all FRBs in the range $9 \leq \mathrm{SNR} \leq 14$ while keeping $\mathrm{SNR_{th}} = 9$ as in the main analysis, and by removing all FRBs with SNR < 15 but accounting for this via setting $\mathrm{SNR_{th}} = 15$. Thus both SNR > 9 and SNR > 14 calculations should present unbiased (but statistically fluctuating) measures of H_0, while the 'half SNR 9–14 arcmin sample will present a biased estimate.

In Fig. A2, the unbiased samples correctly reproduce the simulated true value of H_0 with errors of $\pm 0.5\,\mathrm{km\,s^{-1}\,Mpc^{-1}}$. The biased half 9–14 sample produces H_0 in-between these two values, very close to the simulated truth. Thus while we cannot exclude that missing FRBs in the range $9 \leq \mathrm{SNR} \leq 14$ results in a bias, this bias is smaller than the random deviation in H_0 when using 1000 FRBs. Therefore, we include the six FRBs with $9 \leq \mathrm{SNR} \leq 14$ in our sample, and use $\mathrm{SNR_{th}} = 9$; and we suggest that all near-future FRB surveys do the same.

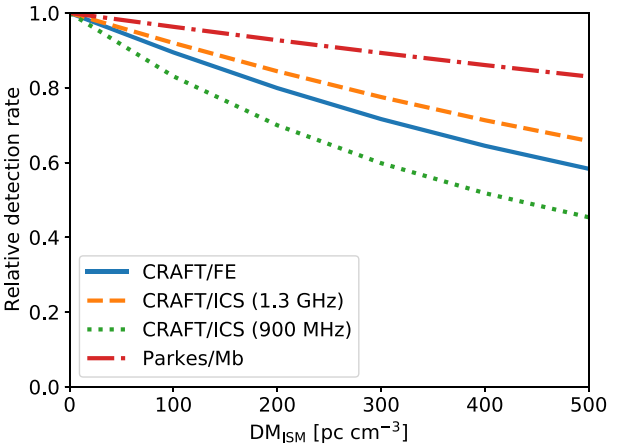

Figure A3. Dependence of total FRB detection rate on $\mathrm{DM_{ISM}}$, relative to the hypothetical rate when $\mathrm{DM_{ISM}} = 0$.

A2 Effect of ISM

The Milky Way interstellar medium (ISM) increases the dispersion measure of extragalactic FRBs at low-Galactic latitudes through an increasing $\mathrm{DM_{ISM}}$. This in turn reduces the sensitivity of FRB surveys at these latitudes in terms of extragalactic dispersion measure, $\mathrm{DM_{EG}}$. Whether or not the apparent paucity of FRBs observed at low-Galactic latitudes by Parkes (Petroff et al. 2014) is due to this effect or e.g. interstellar scintillation (Macquart & Johnston 2015), or is indeed even statistically significant (Bhandari et al. 2018), remains undetermined. Here, we model the effects of $\mathrm{DM_{ISM}}$ on the redshift distribution z of observable FRBs using CRAFT/ICS 1.3 GHz. Note that the Galactic Plane also reduces the ability of optical follow-up observations to identify the FRB host galaxy, as discussed in Section 4.5. Here, we only consider only the effects on the initial detection of FRBs with radio waves.

In Fig. A3, we plot the total (simulated) detectable FRB rate as a function of $\mathrm{DM_{ISM}}$ for the FRB surveys used in this work. In the range of 0–500 $\mathrm{pc\,cm^{-3}}$, the detection rate falls the least (∼20 per cent) for Parkes/Mb, due to its high-frequency resolution negating the effects of increased DM smearing; and the most (∼50 per cent) for

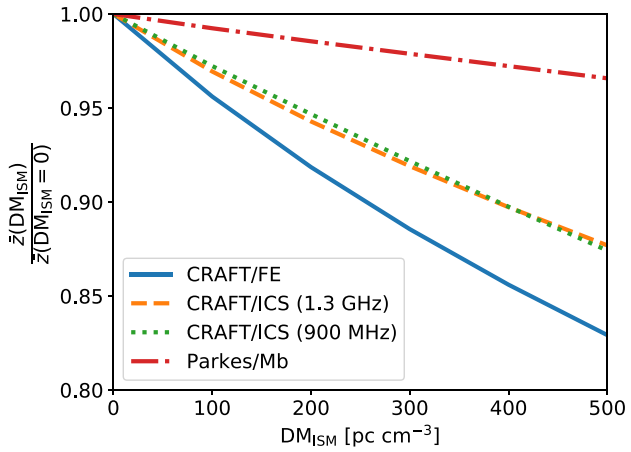

Figure A4. Dependence of mean detected redshift z on $\mathrm{DM_{ISM}}$.

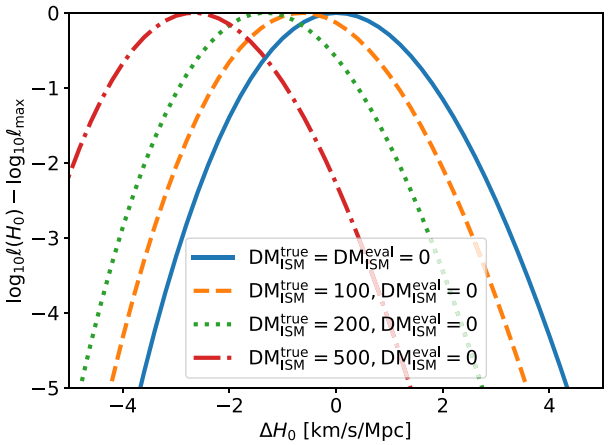

Figure A5. Effect on evaluated likelihoods of H_0 (relative to maximum) when using an incorrect value of $\mathrm{DM_{ISM}}$ for evaluation.

CRAFT/ICS 900 MHz due to its lower observation frequency and hence greater DM smearing.

The effect of this reduced sensitivity on the observable redshift distribution is shown in Fig. A4. An increased $\mathrm{DM_{ISM}}$ decreases the mean redshift of detectable FRBs, $\bar{z}$, for all surveys considered here. Again, Parkes/Mb is the least affected survey. However, the relative effect on CRAFT/FE (17 per cent reduction in $\bar{z}$ at $\mathrm{DM_{ISM}} = 500\,\mathrm{pc\,cm^{-3}}$ relative to $\mathrm{DM_{ISM}} = 0\,\mathrm{pc\,cm^{-3}}$) is now greater than that on CRAFT/ICS 900 MHz. This is likely because the lower sensitivity of CRAFT/FE leads to, on-average, lower values of $\mathrm{DM_{EG}}$, so that a moderate increase in $\mathrm{DM_{ISM}}$ has a proportionally greater effect on sensitivity and hence $\bar{z}$.

To test the effect of this approximation on H_0, we use simulated FRBs from CRAFT/ICS 1.3 GHz and the best-fit parameters of James et al. (2022b). We simulate four sets of FRBs, setting $\mathrm{DM_{ISM}}$ to 0, 100, 200, and 500 pc cm^{-3}. To illustrate the bias effect of $\mathrm{DM_{ISM}}$ on H_0, we evaluate the likelihood ℓ by changing H_0 only, subject to the constraint on $\Omega_b h^2$.

For our first test, we use samples of FRBs with $\mathrm{DM_{EG}}$ generated at true values of $\mathrm{DM_{ISM}}$, $\mathrm{DM_{ISM}^{true}}$ of 0, 100, 200, and 500 pc cm^{-3}, but H_0 is evaluated assuming a different value, $\mathrm{DM_{ISM}^{eval}} = 0$. The results are shown in Fig. A5. In all cases, the most likely value of H_0 is evaluated as being lower, by 0.6, 1.4, and 2.6 km s^{-1} Mpc^{-1} for 100, 200, and 500 pc cm^{-3}, respectively to account for seeing FRBs with lower $\mathrm{DM_{FRB}}$ for a given redshift.

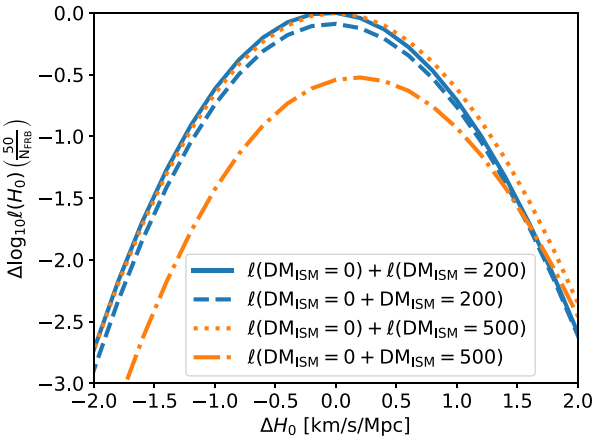

Figure A6. Effect of merging samples with common $\mathrm{DM_{ISM}}$ on H_0.

The effect of $\mathrm{DM_{ISM}}$ on H_0 illustrated in Fig. A5 is accounted-for in our simulation code by subtracting $\mathrm{DM_{ISM}}$ (and $\mathrm{DM_{host}}$) from $\mathrm{DM_{FRB}}$ to calculate $\mathrm{DM_{EG}}$ on a per-event basis. However, the observation bias as a function of $\mathrm{DM_{EG}}$ is calculated using the mean value of $\mathrm{DM_{ISM}}$ for each sample only. This is done purely because generating a z–DM grid for each FRB individually is too computationally expensive.

To test the effect of mixing FRBs with different values of $\mathrm{DM_{ISM}}$ into the same evaluation, we take samples of FRBs generated at $\mathrm{DM_{ISM}} = 200$ and 500 pc cm^{-3}, and add them to the sample generated at $\mathrm{DM_{ISM}} = 0\,\mathrm{pc\,cm^{-3}}$. H_0 is then evaluated using the default method of averaging $\mathrm{DM_{ISM}}$ over the sample, i.e. to $\mathrm{DM_{ISM}} = 100$ and $\mathrm{DM_{ISM}} = 250\,\mathrm{pc\,cm^{-3}}$, respectively. This is compared to results on H_0 generated by treating samples at $\mathrm{DM_{ISM}} = 0$, 200, and 500 pc cm^{-3} individually, i.e. such that the average value of $\mathrm{DM_{ISM}}$ is the correct one. Results are shown in Fig. A6 giving the shift in most likely value of H_0, and the change in maximum likelihood $\ell_{\max}$ per 50 events (the vertical shift in maximum likelihood over 2000 events can be quite large, and prevents easy display). The effect of averaging $\mathrm{DM_{ISM}}$ over 0 and 200 pc cm^{-3} is negligible, resulting in bias of only $+0.027\,\mathrm{km\,s^{-1}\,Mpc^{-1}}$. Mixing samples of FRBs with $\mathrm{DM_{ISM}}$ between 0 and 500 pc cm^{-3} is less reliable with a bias of $0.18\,\mathrm{km\,s^{-1}\,Mpc^{-1}}$.

These biases are currently significantly smaller than the random errors from our small sample of localized FRBs, especially given that all have been detected with $\mathrm{DM_{ISM}} < 200\,\mathrm{pc\,cm^{-3}}$. Thus we loosen the constraint of $\mathrm{DM_{ISM}} < 100\,\mathrm{pc\,cm^{-3}}$ previously adopted in James et al. (2022a), and include all FRBs localized by ASKAP in our main analysis. It also allows us to include ASKAP/FE and Parkes/Mb FRBs originally excluded from the sample of James et al. (2022a), which are listed in Table 3.

A3 Effect of unlocalized ASKAP/ICS FRBs

The majority of ASKAP/ICS FRBs have had their host galaxies, and hence redshifts identified. However, several FRBs remain unlocalized, as described in Section 4.5. These reasons generally fall into two categories: reasons uncorrelated with FRB properties, which result in reduced statistical power on H_0 but no potential bias; and those which are correlated with FRB properties, and thus could potentially bias a study such as that presented in this work.

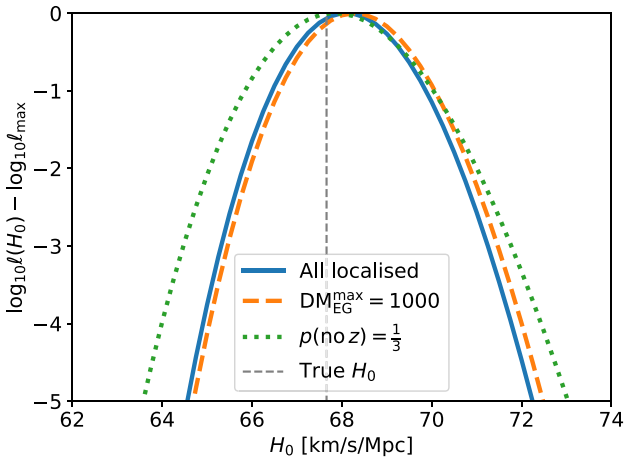

Figure A7. Constraints on H_0 obtained from 1000 synthetic (Monte Carlo) FRBs when varying H_0 only assuming all bursts are localized; when discarding all 30 bursts with $DM_{EG} > DM_{EG}^{max} = 1000\,pc\,cm^{-3}$; and when also discarding one third of FRBs chosen randomly. No bias is visible when estimating H_0, but some loss of accuracy is, as expected.

In particular, the sample used in this work includes two FRBs with DM over $1000\,pc\,cm^{-3}$ (FRB 20210407 and FRB 20210912) with potentially high-redshift host galaxies which have not been identified in initial follow-up observations with the VLT, although in the former case Galactic extinction plays a significant role. If DM_{FRB} is dominated by DM_{cosmic} therefore, the hosts of these FRBs will lie at $z \gtrsim 1$ and may not be detectable with standard follow-up observations. However, if DM_{FRB} is dominated by a large host contribution, such as FRB 20210117A (Bhandari et al. (in prep.)), the host will be readily identified. This then leads to a sample biased towards low redshift.

To counter this effect, we place an upper limit on DM_{EG}, DM_{EG}^{max}, below which we expect all FRB hosts to be identifiable. Above DM_{EG}^{max}, we discard all redshift information, even if known. We also include the DM of FRBs that remain unlocalized for observational reasons. This implementation has been tested using Monte Carlo FRBs generated from the CRAFT/ICS 1.3 GHz survey parameters, as per Appendix A2. Results are shown in Fig. A7. Clearly, the loss of information when removing FRB redshifts results in poorer statistical constraints on H_0, however, no systematic bias has been introduced.

A4 Effects of gridding in z–DM space

The probability distribution $P(z, \mathrm{DM})$ is calculated on a finite grid of $N_z = 500$, linearly spaced redshifts up to $z = 5$, and $N_{DM} = 1400$, linearly spaced dispersion measures up to $DM = 7000\,pc\,cm^{-3}$. Furthermore, we parametrize the telescope beamshape using only $N_b = 5$ combinations of beam sensitivity B and solid angle $\Omega(B)$. To test the effects of this choice of gridding, we again calculate $p(H_0|s, z, \mathrm{DM})$ for different gridding choices using the simulated CRACO sample while holding all other parameters fixed. The results are shown in Fig. A8.

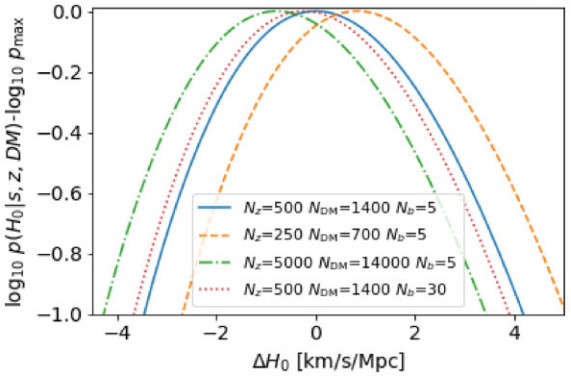

Figure A8. Simulated systematic effect on H_0 estimates using the CRACO due to the number of redshifts N_z, DMs N_{DM}, and beam values N_b. Shown is the posterior probability distribution $\log_{10} p(H_0|s, z, \mathrm{DM})$ normalized to the maximum value, as a function of ΔH_0, i.e. the deviation from the best-fitting value of H_0 obtained for the default grid of $N_{DM} = 1400$, $N_z = 500$, and $N_b = 5$.

We find that our best-fitting value of H_0 varies by $\pm 1\,km\,s^{-1}\,Mpc^{-1}$, according to our choice of gridding: for this particular sample, a grid sparser by a factor of two ($N_z = 250$, $N_{DM} = 700$) produces a higher value of H_0 by $1\,km\,s^{-1}\,Mpc^{-1}$, while ten-fold finer grid ($N_z = 5000$, $N_{DM} = 14000$) produces a lower value of H_0 by $1\,km\,s^{-1}\,Mpc^{-1}$. Increasing N_b has almost no effect on the estimation of H_0, which is likely due to this parameter being extensively optimized by J22a.

We attribute this sensitivity to two regions of parameter space that are sensitive to smoothness, being the sharp decline in $P(\mathrm{DM}|z)$ near the lower boundary due to the cliff effect, and the low-z region.

Compared to our current uncertainty in H_0 estimates with FRBs, a potential systematic error of $\pm 1\,km\,s^{-1}\,Mpc^{-1}$ is small. However, in future, this suggests either using a finer grid in z–DM space; optimising the spacing, e.g. using log-spaced grids; or shifting to a method which does not use a brute force calculation over a grid, but performs a more intelligent optimization of parameters.

This paper has been typeset from a TEX/LATEX file prepared by the author.